

Magnetic and transport dc properties of inductive Josephson-junction arrays

Daniel Domínguez*

Theoretical Division, Los Alamos National Laboratory, T-11, Los Alamos, New Mexico 87545

Jorge V. José

Physics Department and Center for the Interdisciplinary Research on Complex Systems, Northeastern University, Boston, Massachusetts 02115

(Received 4 August 1995)

We present an extensive study of the dc magnetic and transport properties of inductive Josephson junction arrays at zero temperature. We carry out the analysis using the resistively shunted Josephson junction (RSJ) model plus Faraday's law. We explicitly discuss the gauge invariance of the equations as well as their symmetries. We consider and compare the results of three different models for the corresponding inductance matrix: self-inductance, nearest-neighbor inductance, and full inductance matrix. The importance of carefully considering the boundary conditions for external currents is discussed as well. Heuristic analytic results are derived from linearizing the RSJ plus Faraday's law equations. In particular, we discuss the critical properties of the model and the nature of the vortex-vortex interactions when going from negligible to strong screening regimes. The dc properties of the arrays are analyzed as a function of the screening parameter $\kappa = \lambda/a$, with λ the magnetic penetration depth and a the lattice spacing. The weak or extreme type II regime corresponds to $\kappa \gg 1$, and the strong screening or type I regime to $\kappa \leq 1$. We present results for the calculated magnetization and vortex densities as a function of external magnetic fields for a set of κ 's and lattice sizes. A qualitative change is found between the dc magnetic and transport responses of the inductive Josephson arrays when going from the type II to the type I regime.

I. INTRODUCTION

Two-dimensional arrays of Josephson junctions have been extensively studied in the last few years.^{1,2} Modern photolithographic techniques have allowed the fabrication of these arrays with tailor made properties. They were initially fabricated as model systems to study the Berezinskii-Kosterlitz-Thouless (BKT) phase transition.^{3,4} In recent years the interest has shifted to studying their dynamical properties.⁵⁻⁷ These studies extend the well studied resistively shunted junction (RSJ) model to describe the dynamics of a single Josephson junction⁸ to the whole Josephson-junction array (JJA), plus Kirkhoff current conservation conditions.⁵ Recent experiments on fractional giant Shapiro steps⁹⁻¹¹ have been successfully interpreted using this model for the array dynamics.¹²⁻¹⁸

In both RSJ dynamical studies and equilibrium thermodynamical studies,^{1,4} the effect of self-induced magnetic fields (SIMF's) was neglected. This assumption takes the total magnetic field \mathbf{B} equal to the externally applied field \mathbf{H}_{ext} , which is valid whenever the array penetration depth λ is larger than the array size.¹⁹ For most arrays studied experimentally near the BKT transition this is a good approximation.⁴ However, at lower temperatures, λ decreases and it can even become on the order of the lattice constant a . This situation was found to be relevant in some of the recent experiments in giant Shapiro steps.¹⁰ We have explained some features of these experiments using the RSJ dynamical model that included SIMF effects.^{16,17} In this paper we plan to study the magnetic properties and the IV characteristics of *inductive* Josephson-junction arrays (IJJA's), i.e., JJA's in which the effect of SIMF's is strong

($\lambda \sim a$), using the models for different approximations to the inductance matrix used in Ref. 17.

Other authors have also included the SIMF effects in their dynamical studies. Nakajima and Sawada²⁰ studied vortex motion in JJA's with screening. Majhofer, Wolf, and Dieterich²¹ studied irreversible magnetic properties of IJJA's related to high- T_c superconductivity. Both these studies included only the self-inductance contribution to the SIMF. This local approximation is equivalent to the one used by Minnhagen in his study of the Coulomb gas with screening.²² Later on we showed¹⁶ that at least the nearest-neighbor inductance contributions have to be included in order to interpret the experimental observations of Lee *et al.* in Ref. 10. However, any realistic calculation of the SIMF effects has to include the full inductance matrix. Stroud and Kivelson²³ calculated the effective vortex-vortex interaction in IJJA's taking into account the long-range contributions to the inductance matrix. They showed that the interaction energy decreases as $1/r$ for $r \gg \lambda$ and $r \gg a$, in analogy with the screening effects found by Pearl²⁴ for superconducting thin films. Also Orlando *et al.*²⁵ have presented a phenomenological discussion of the dynamical properties of vortices in a continuum limit of a JJA. Recently, Phillips *et al.*²⁶⁻²⁸ were able to do calculations of static and dynamic vortex properties of IJJA's, taking into account the full inductance matrix contributions to the SIMF's. They showed that, depending on the use of a local approximation for the inductance or the full inductance matrix, there are differences in the long-range magnetic field and current distributions for vortices. In particular, this can affect the quantitative value of the critical field for the nucleation of one vortex inside the array.²⁶ Also the full inductance matrix has been considered by Reinel *et*

*al.*²⁹ and by us¹⁷ in current-driven arrays. Hagenaaers *et al.*³⁰ have used the full inductance matrix in IJJA's (in the same way as considered here and in Ref. 17), making a successful comparison with recent experiments by Lachenmann *et al.*³¹ There have also been studies of SIMF effects in superconducting wire networks when analyzing their thermodynamic and magnetic properties.^{32–34} Recent simulations of the time-dependent Ginzburg-Landau equation for continuous superconductors³⁵ are equivalent to the diagonal approximation of Refs. 20 and 21 in IJJA's (i.e., they neglect demagnetization effects in two-dimensional superconductors), when considering the magnitude of the order parameter constant. The effect of a finite penetration depth has also been taken into account in recent three-dimensional simulations relating to high-temperature superconductors: on the vortex lattice melting transition,³⁶ on the nature of the vortex-glass transition,³⁷ and on the existence of a paramagnetic Meissner effect.³⁸ All these three-dimensional simulations are also equivalent to a diagonal approximation of the inductance matrix, believed to be a more accurate approach in three-dimensional (3D) Josephson-junction arrays (see also Ref. 39 for an application to giant Shapiro steps in 3D JJA's).

Here we study the magnetic properties and the *IV* characteristics of IJJA's at $T=0$.⁴⁰ We present calculations of the dynamical behavior of the arrays based on the RSJ model. We include the SIMF effects using either a local approximation or the full inductance matrix, emphasizing their similarities and differences. One of our main results is that there is unusual physical behavior of the IJJA for strong screening ($\lambda \lesssim a$), regardless of the inductance matrix model used. This behavior resembles a type I superconductor in many respects. For high fields our results can be described in terms of an extension of the Bean model⁴¹ for hard superconductors to discrete arrays. We show that this regime for IJJA's is caused by the existence of an effective attractive interaction between vortices for $\lambda \ll a$.

The paper is organized as follows. In Sec. II we present the model equations that describe the self-consistent nature of the dynamics of the arrays. In Secs. II A and II B we discuss the equations in two different gauges. In Sec. II C we define the three models for the inductance matrix considered here, to wit, model A for a self-inductance, model B for a self-plus nearest-neighbor inductance matrix approximation, and model C for the full inductance model. In Sec. II D we define the physical quantities calculated in our work. We also discuss the relation between the inductance matrix and the array's penetration depth (Sec. III), and the effective vortex-vortex interaction in the Coulomb gas approximation (Sec. III B). Section IV is devoted to the study of the magnetic properties of the IJJA. We focus on the dynamical behavior for the magnetic field (and vortex) penetration from the array boundaries. In Sec. IV A we discuss the case for $\lambda \gtrsim a$, while in Sec. IV B we show results for $\lambda \lesssim a$, and we describe this type-I-like regime for IJJA's. Section IV C considers the nature of the vortex-vortex interactions in the type I regime, which turn out to be attractive as compared to being repulsive in the type II regime. In Sec. IV D we present a lattice version of the Bean model that helps understand the importance of lattice pinning in the behavior of the IJJA in this regime. In Sec. IV E we calculate the critical fields for vortex penetration from the boundaries. Then in

Sec. IV F we discuss the irreversible magnetic behavior of IJJA's in both regimes, relating to the previous work done by Majhofer, Wolf, and Dieterich.²¹ Section V deals with the behavior of the IJJA driven by a dc current. In Sec. V A we show how the dynamical equations given in Sec. II B have to be modified in order to include the external driving current. This leads naturally to the presence of *antisymmetric edge magnetic fields* induced by the external currents. In Sec. V B we discuss some aspects of the *IV* characteristics and vortex states of the current-driven IJJA. Finally, in Sec. VI we restate our main conclusions. There are also three appendixes that discuss important technical considerations of the model and calculations carried out in this paper. In Appendix A we discuss the symmetries of the Hamiltonian studied in this paper. In Appendix B we discuss the different algorithms used to obtain our results. Appendix C clarifies the differences between the results obtained using different boundary conditions for the currents fed into the IJJA.

II. THE MODEL

A Josephson-junction array (JJA) is made of an $N \times N$ network of superconducting islands connected by Josephson currents.^{1,2,4} We use the RSJ model⁸ for the current through the junction that goes from r to $r + \mu$ ($\mu = \hat{e}_x, \hat{e}_y$):

$$I_\mu(r) = I_0 \sin[\Delta_\mu \theta(r) - A_\mu(r)] + \frac{\Phi_0}{2\pi\mathcal{R}} \frac{d}{dt} [\Delta_\mu \theta(r) - A_\mu(r)]. \quad (1)$$

Here, $\Delta_\mu \theta = \theta(r + \mu) - \theta(r)$ and $A_\mu(r) = (\Phi_0 / 2\pi) \int_r^{r+\mu} \vec{\mathbf{A}} \cdot d\vec{\mathbf{l}}$, where I_0 is the junction's critical current, \mathcal{R} is the shunt resistance, and $\Phi_0 = h/2e$ is the quantum of flux.

The Kirchhoff, or current conservation, conditions are

$$\Delta_\mu \cdot I_\mu(r) = I_x(r) - I_x(r - e_x) + I_y(r) - I_y(r - e_y) = 0, \quad (2)$$

which imply that we can write $I_\mu(r)$ as the lattice curl of a "mesh current" $J(R)$, defined on the dual lattice sites $R = (r_x + e_x/2, r_y + e_y/2)$,

$$I_x(r) = J(R) - J(R - e_y),$$

$$I_y(r) = J(R - e_x) - J(R),$$

or, in shorthand notation,

$$I_\mu(r) = \Delta_\mu \times J(R). \quad (3)$$

Here we have defined $J(R)$ as positive when the current around the mesh R flows in the anticlockwise direction.

Note that including the self-fields in the current $I_\mu(r, t)$ along the bonds of the lattice implies that

$$\frac{dA_\mu(r, t)}{dt} \neq 0,$$

where the vector potential $A_\mu(r, t)$ is related to the *total* magnetic flux $\Phi(R, t)$ at plaquette R by

$$\begin{aligned} \frac{2\pi\Phi(R,t)}{\Phi_0} &= A_x(r,t) + A_y(r + \hat{e}_x, t) - A_x(r + \hat{e}_y, t) - A_y(r,t) \\ &= \Delta_\mu \times A_\mu(r,t). \end{aligned} \quad (4)$$

In this case the total $\Phi(R,t)$ now depends on the flux generated by the external field $\Phi_x = Ha^2 = f\Phi_0$, plus the magnetic flux induced by all the currents flowing in the array. Specifically we can write

$$\Phi(R,t) = \Phi_x(R) + \sum_{r',\mu'} \Gamma(R,r',\mu') I_{\mu'}(r',t), \quad (5)$$

where $\Gamma(R,r',\mu')$ is a matrix that explicitly depends on the geometries of the array and the junctions. It is convenient to write Eq. (5) only in terms of dual or plaquette variables.

In terms of the plaquette variables Eq. (5) can now be written as

$$\Phi(R,t) = \Phi_x(R) + \sum_{R'} L(R,R') J(R',t) \quad (6)$$

where

$$L(R,R') = \Delta_\mu \cdot \Gamma(R,r',\mu') \quad (7)$$

is the inductance matrix of the array.

A. Coulomb gauge

We note that to write down the set of dynamical equations for $A_\mu(r,t)$ and $\theta(r,t)$ we need to fix a gauge. In the Coulomb gauge,

$$\Delta_\mu \cdot A_\mu(r) = 0, \quad (8)$$

with the boundary condition

$$A_n(\text{boundary}) = 0, \quad (9)$$

with n the direction normal to the boundaries. Taking $\Delta_\mu \cdot I_\mu(r)$ in Eqs. (1), and using Eqs. (2) and (8), we get

$$\Delta_\mu^2 \frac{d\theta(r)}{dt} = - \frac{2\pi\mathcal{R}I_0}{\Phi_0} \Delta_\mu \cdot \sin[\Delta_\mu \theta(r) - A_\mu(r)], \quad (10)$$

with $\Delta_\mu^2 = \Delta_\mu \cdot \Delta_\mu$ the discrete two-dimensional Laplacian. This equation can be inverted using

$$\Delta_\mu^2 G(r,r') = -\delta_{r,r'}, \quad (11)$$

where $G(r,r')$ is the two-dimensional lattice Green function. The dynamical evolution equation for the phase $\theta(r)$ is then given by

$$\frac{d\theta(r)}{dt} = \frac{2\pi\mathcal{R}I_0}{\Phi_0} \sum_{r'} G(r,r') \Delta_\mu \cdot \sin[\Delta_\mu \theta(r) - A_\mu(r)]. \quad (12)$$

This is the same system of equations used to study the RSJ dynamics of a JJA without screening as in, for example, Refs. 5 and 6. The difference is that now $A_\mu(r)$ is a dynamical variable. Therefore we have to complement Eq. (12) with a set of equations for the dynamics of the electromagnetic field variables.

Let us describe the dynamics of the magnetic field in terms of $\Phi(R)$. Taking $\Delta_\mu \times I_\mu(r)$ in Eq. (1), and using Eq. (4), we get

$$\frac{d\Phi(R)}{dt} = \mathcal{R}I_0 \Delta_\mu \times \sin[\Delta_\mu \theta(r) - A_\mu(r)] - \mathcal{R} \Delta_\mu \times I_\mu(r). \quad (13)$$

Now, taking $\Delta_\mu \times$ on Eq. (3), and solving for $J(R)$ from Eq. (6), we finally arrive at

$$\begin{aligned} \frac{d\Phi(R,t)}{dt} &= \mathcal{R}I_0 \Delta_\mu \times \sin[\Delta_\mu \theta(r,t) - A_\mu(r,t)] \\ &\quad + \mathcal{R} \Delta_\mu^2 \left[\sum_{R'} L^{-1}(R,R') (\Phi(R',t) - \Phi_x) \right]. \end{aligned} \quad (14)$$

To close this system of equations, we need to get $A_\mu(r)$ from $\Phi(R)$. This can be done using Eq. (4) and Eq. (8) which, after some algebra, gives

$$A_\mu(r) = \Delta_\mu \times \sum_{R'} \tilde{G}(R,R') \Phi(R'), \quad (15)$$

where $\tilde{G}(R,R')$ is the two-dimensional Green function of the dual lattice.

The full dynamics of a JJA with screening is then governed by Eq. (12) together with Eq. (14). The advantage of using the Coulomb gauge is that the dynamics of the phase θ and the magnetic flux Φ can be followed separately. Using this gauge will be useful when discussing the relevant characteristic lengths and time scales in Secs. III and III B. However, from the computational point of view it is more efficient to use the temporal gauge, which we present in the next subsection.

B. Temporal gauge

The temporal gauge has been extensively used in condensed matter physics in the past,⁴² and recently in Refs. 21, 16, 26, and 35. In this gauge we choose as the dynamical variable the gauge-invariant phase difference

$$\Psi_\mu(r) = \Delta_\mu \theta(r) - A_\mu(r). \quad (16)$$

This can be thought of as a gauge in which we set $\Delta_\mu \theta(r) = 0$, and therefore $\Psi_\mu(r) = -A_\mu(r)$. In this gauge Eq. (1) becomes

$$\frac{d\Psi_\mu(r)}{dt} = - \frac{2\pi\mathcal{R}I_0}{\Phi_0} \sin\Psi_\mu(r) + \frac{2\pi\mathcal{R}}{\Phi_0} I_\mu(r). \quad (17)$$

Substituting $J(R)$ from Eq. (6) in Eq. (3) we get for $I_\mu(r)$

$$I_\mu(r) = \Delta_\mu \times \sum_{R'} L^{-1}(R,R') [\Phi(R') - \Phi_x]. \quad (18)$$

Combining Eq. (16) with Eq. (4), the total magnetic flux is

$$\Phi(R) = - \frac{\Phi_0}{2\pi} \Delta_\mu \times \Psi_\mu(r), \quad (19)$$

where we have taken $\Delta_\mu \theta(r)$ as a variable in $[-\infty, \infty]$ and, therefore, $\Delta_\mu \times \Delta_\mu \theta(r) = 0$. We arrive at the following set of JJA dynamical equations in the temporal gauge:

$$\frac{d\Psi_\mu(r)}{dt} = -\frac{2\pi\mathcal{R}I_0}{\Phi_0} \sin\Psi_\mu(r) - \mathcal{R}\Delta_\mu \times \sum_{R'} L^{-1}(R, R') \times \left(\Delta_\mu \times \Psi_\mu(r') + \frac{2\pi}{\Phi_0} \Phi_x \right). \quad (20)$$

This system of equations is easier to compute numerically than Eqs. (12), (14), and (15), but has the disadvantage that the dynamics of the phase and the magnetic field are not separated. Therefore it can be used when the characteristic times of both variables are not too different.

C. Inductance matrix models

A general analytic expression for the inductance matrix $L(R, R')$, valid for arbitrary (R, R') and array geometry, is not known. However, we can learn a lot about the main qualitative properties of the array from the asymptotic properties of $L(R, R')$ and its general symmetries. We start by writing the standard definition of the $\Gamma(R, r', \mu')$ matrix defined in Eq. (5),

$$\Gamma(R, r', \mu') = \frac{\mu_0}{4\pi} \frac{1}{S_R S_{r'\mu'}} \oint_R \int_{r'\mu'} \frac{d\vec{\mathbf{l}}_R \cdot d\vec{\mathbf{l}}_{r'\mu'} dS_R dS_{r'\mu'}}{|\vec{\rho}_R - \vec{\rho}_{r'\mu'}|}. \quad (21)$$

Here, S_R and $S_{r'\mu'}$ are the cross sectional areas of the junctions in the plaquette R and the branches r' and μ' , respectively. The integrals are along the links between superconducting islands. This expression for Γ makes explicit its dependence on the geometrical characteristics of the array and the junctions. Using Eq. (7), the representation of $L(R, R')$ based on Eq. (21) gives

$$L(R, R') = \frac{\mu_0}{4\pi} \frac{1}{S_R S_{R'}} \oint_R \oint_{R'} \frac{d\vec{\mathbf{l}}_R \cdot d\vec{\mathbf{l}}_{R'} dS_R dS_{R'}}{|\vec{\rho}_R - \vec{\rho}_{R'}|}. \quad (22)$$

This expression depends on the particular shape of the junctions and geometry of the JJA. Here we note that the general qualitative properties of the response of the array to external probes will not depend on the detailed form of the full inductance matrix.

The relevant properties of $L(R, R')$, independent of the specific array geometry, are that (i) $L(R, R')$ is a definite positive matrix, with its diagonal element positive and its off-diagonal elements negative, (ii) the condition $\sum_{R'=-\infty}^{\infty} L(R, R') = 0$ must be fulfilled, because of continuity of the magnetic flux lines (the sum includes *all* the R' , even outside the array), and (iii) for large distances one can approximate the lattice problem by its continuum limit, leading to

$$L(R, R')|_{|R-R'| \gg a} \approx -\frac{\mu_0}{4\pi} \frac{a^4}{|R-R'|^3}, \quad (23)$$

which corresponds to the field of a three-dimensional magnetic dipole produced by a current loop. Note that the long-

range behavior of $L(R, R')$ is always given by Eq. (23), for it is independent of the particular shape of the junctions.

On the other hand, the short-distance properties of the $L(R, R')$ matrix depend explicitly on the specific geometry of the junctions. Here we use the results of a short-distance asymptotic evaluation of $L(R, R')$ obtained by direct integration of Eq. (22) for a square network of cylindrical wires.^{34,29} For example, the local behavior of $L(R, R')$ is found to be given by

$$L(R, R) = L_0 = \frac{\mu_0 a}{2\pi} \left[8 \ln \frac{2a}{r(1+2\sqrt{2})} + 8\sqrt{2} - 14 \right],$$

$$L(R, R \pm \mu) = -M = -\frac{1}{4} L_0 + \frac{\mu_0 a}{2\pi} 0.141875, \quad (24)$$

$$L(R, R \pm e_x \pm e_y) = -M_{11} = -\frac{\mu_0 a}{2\pi} 0.4 \dots,$$

where a is the lattice constant and r is the radius of the wires. For the JJA we take $2r$ as the typical width of the junctions.

We emphasize here that there are *two parameters* that must be given to adequately specify the inductance matrix: (1) $\mu_0 a$, which determines the ‘‘strength’’ of the screening effects and the long-range behavior of $L(R, R')$ (it determines the penetration depth λ , as we will see below), and (2) a/r , which determines the short-range screening effects, i.e., the relative strengths of the local inductances as compared with their long-range counterparts.

From now on we normalize the inductance matrix elements by $\mu_0 a$, or $\Lambda(R, R') = L(R, R')/\mu_0 a$, $\Lambda_0 = L_0/\mu_0 a$, and $\mathcal{M} = M/\mu_0 a$. We use $a/r = 10$, which is a typical value for arrays made with superconductor-normal-metal-superconductor (SNS) junctions,¹⁰ for which $\Lambda_0 = 1.13 \dots$, $\mathcal{M} = 0.14 \dots$, $\mathcal{M}_{11} = 0.064 \dots$. [This same value was used in Refs. 17, 29, and 30, whereas $a/r = 4$, typical of superconductor-insulator-superconduction (SIS) junction arrays, was used in Refs. 26–28.]

We have introduced three different models for the inductance matrix that depend on its range.

Model A includes screening effects to $L(R, R')$ only at the diagonal or self-inductance component level, i.e.,

$$L(R, R') = \Lambda_0 \mu_0 a \delta_{R, R'}. \quad (25)$$

This is the simplest approximation that leads to zero edge magnetic fields. Model A has been used in the past by Nakajima and Sawada²⁰ to study vortex motion, and by Majhofer *et al.*²¹ to model irreversible properties of ceramic superconductors. This model is good when trying to describe the properties of bulk samples, in three-dimensional arrays.^{39,38}

Model B improves on model A in that it includes the nearest-neighbor mutual inductance contributions to the diagonal one:

$$L(R, R') = \Lambda_0 \mu_0 a \delta_{R, R'} - \mathcal{M} \mu_0 a \delta_{R, R' \pm \mu}. \quad (26)$$

This model was introduced by us to study screening effects on the nucleation of giant Shapiro steps.¹⁶

Model C includes the *full-range* inductance matrix in the calculations. We model $L(R, R')$ in this case by taking into account the local geometry of the junctions in the diagonal and mutual inductance contributions, as specified in Eq. (24), using the filamentary wire approximation for the remaining terms.

The inclusion of the full-range inductance matrix in the study of JJA's was considered by Phillips *et al.*,²⁶ who developed an efficient algorithm to study static vortex properties in JJA's. Also Reinel *et al.*²⁹ recently implemented a full inductance matrix approach to calculate static and dynamic properties, somewhat closer in spirit to the method we used to study the dynamic response of the JJA.¹⁷ Phillips *et al.*²⁷ have extended their static approach to study the dynamic response of JJA's. We will compare our results for models A through C to theirs where appropriate.

Note that the essential difference between models A, B, and C is that A and B assume that the magnetic field lines are constrained to lie on the plane while C fully takes into account the three-dimensionality of the physical problem. However, in the limit of very narrow junctions, $r \ll a$, the local inductances become dominant [because of the $\ln(a/r)$ terms in Eq. (24)], and model B with $L_0 \approx -4M$ becomes an accurate approximation to model C.

The complexity of the algorithms needed to solve the dynamical equations grows with the range of the inductance matrix. We discuss the specific details of the implementation of these algorithms in Appendix C.

D. Physical variables calculated

We calculate the distribution of normalized total magnetic flux in the arrays as a function of time, $\phi(R, t) = \Phi(R, t)/\Phi_0$, from which we get the average magnetization

$$m = \frac{1}{(N-1)^2 T} \sum_R \sum_{t=0}^{T-1} \phi(R, t) - f, \quad (27)$$

as a function of the external field $f = \Phi_x/\Phi_0$. We also have calculated the distribution of vortices $n(R, t)$. The vorticity is defined as the number 2π of "turns" of the gauge-invariant phase difference around a plaquette. This corresponds to $2\pi[n - \phi(R)] = \Delta_\mu \times \tilde{\Psi}_\mu(r)$, with $\tilde{\Psi}_\mu(r) = \Psi_\mu(r) - 2\pi \text{nint}[\Psi_\mu(r)/2\pi]$ the gauge-invariant phase difference restricted to the $[-\pi, \pi]$ interval, and $\text{nint}(x)$ giving the nearest integer to x . Then we evaluate the vorticity as

$$n(R, t) = -\Delta_\mu \times \text{nint}\left(\frac{\Psi_\mu(r, t)}{2\pi}\right). \quad (28)$$

From this we get the average vortex density

$$q = \frac{1}{(N-1)^2 T} \sum_R \sum_{t=0}^{T-1} n(R, t). \quad (29)$$

In Sec. V we also calculate the electric response as a function of the driving dc current I_{ext} . If the current is applied in the y direction, we calculate the average voltage difference as

$$v = \frac{1}{N(N-1)T} \sum_r \sum_{t=0}^{T-1} \frac{d\Psi_y(r, t)}{dt}, \quad (30)$$

where the voltage is normalized as $v = V/\mathcal{R}I_0$.

III. GENERAL LINEARIZED RESULTS

An analytic detailed study of the full dynamical equations is out of the question. However, a number of relevant qualitative results can be obtained from analyzing these equations in their linearized approximation. In this section we calculate the magnetization and the vortex-vortex interaction potential in the linearized approximation.

A. Magnetization

In a periodic array we have translational invariance; then $\Lambda(R, R') = \Lambda(R - R')$. It is useful to know the Fourier transform of the inductance matrix, $\Lambda(\vec{q}) = \sum_R \Lambda(R) e^{iqR}$. Since also $\Lambda(R) = \Lambda(-R)$, $\Lambda(q)$ has to be an even function of q .

For a short-range matrix, as in model A, we can power series expand $\Lambda(q)$ as

$$\Lambda(\vec{q})_{q \rightarrow 0} = \bar{\Lambda} + \Lambda_2 q^2 a^2 + O(q^4). \quad (31)$$

However, for model C, we see that $\lim_{N \rightarrow \infty} \bar{\Lambda} = \sum_R \Lambda(R) = 0$, due to the long-range nature of $\Lambda(R)$, and the q^4 term diverges. Instead, by taking the long-range behavior of the matrix as $1/R^3$, Eq. (23), one can estimate the Fourier transform for small wave vectors as

$$\Lambda(\vec{q})_{q \rightarrow 0} \approx |\vec{q}| a. \quad (32)$$

We now can estimate how $\Lambda(R, R')$ determines the characteristic lengths and times by linearizing the dynamical equations. This means approximating $\sin[\Delta_\mu \theta(r) - A_\mu(r)] \approx \Delta_\mu \theta(r) - A_\mu(r)$. In order to keep track of the periodicity of the sine function, we will take $\Delta_\mu \times \Delta_\mu \theta(r) = 2\pi n(R)$, by compactifying $\Delta_\mu \theta(r)$ within the interval $[-\pi, \pi]$. This defines the *vorticity* $n(R)$, with n an integer. We use the Coulomb gauge in order to separately study the phases and the magnetic flux variables.

Within the linear approximation Eq. (12) reduces simply to

$$\frac{d\theta(r)}{dt} = -\frac{2\pi \mathcal{R}I_0}{\Phi_0} \theta(r), \quad (33)$$

defining the relaxation time of the phases by $\tau_\theta = \Phi_0/2\pi \mathcal{R}I_0$.

The linear approximation of Eq. (14) for the magnetic flux gives

$$\begin{aligned} \frac{d\phi(R)}{dt} &= \frac{1}{\tau_\theta} [n(R) - \phi(R)] \\ &+ \frac{1}{\tau_\Phi} \Delta_\mu^2 \sum_{R'} \Lambda^{-1}(R, R') [\phi(R') - f(R')], \end{aligned} \quad (34)$$

where $\phi(R) = \Phi(R)/\Phi_0$. This equation has two characteristic relaxation times, τ_θ and $\tau_\Phi = \mu_0 a / \mathcal{R}$. In the particular case of model A, $\Lambda(R, R') = \Lambda_0 \delta_{R, R'}$, Eq. (34) reduces to

$$\frac{d\phi(R)}{dt} = \frac{1}{\tau_\theta} [n(R) - \phi(R)] + \frac{1}{\tau_\Phi \Lambda_0} \Delta_\mu^2 [\phi(R) - f], \quad (35)$$

where we could have defined $\tau_\Phi^* = \Lambda_0 \tau_\Phi = L_0 / \mathcal{R}$. Since Λ_0 is of order unity, it is just a matter of taste which one we choose as the magnetic characteristic time. In this paper we will work with τ_Φ .⁴³

We can estimate the characteristic magnetic length, in the stationary limit of Eq. (34), i.e., $d\phi(R)/dt \rightarrow 0$. In this case we have

$$\frac{\tau_\theta}{\tau_\Phi} \Delta_\mu^2 \sum_{R'} \Lambda^{-1}(R, R') [\phi(R') - f] = \phi(R) - n(R). \quad (36)$$

In particular, it is easy to get the characteristic magnetic length in model A since Eq. (36) reduces to

$$\frac{\tau_\theta}{\tau_\Phi \Lambda_0} \Delta_\mu^2 \phi(R) = \phi(R), \quad (37)$$

which is the lattice version of the London equation for the magnetic field.⁴⁴ (Here we have taken the solution without vortices [$n(R) = 0$], and we put $\Delta_\mu^2 [\phi(R) - f] = \Delta_\mu^2 \phi(R)$, which is true everywhere except at the boundaries, where $\phi(R) = f$.) Then the characteristic length in this case is the Josephson penetration depth $\lambda_J = (\tau_\theta / \tau_\Phi \Lambda_0)^{1/2} a$. We define the dimensionless parameter for this case $\kappa_J = \lambda_J / a = (\tau_\theta / \tau_\Phi \Lambda_0)^{1/2}$.

In the more general case, we evaluate the Fourier transform of Eq. (36); defining $\phi(q) = \sum_R \phi(R) e^{iqR}$, we get

$$\phi(q) = \frac{n(q)}{1 + (\tau_\theta / \tau_\Phi) [D(q) / \Lambda(q)]}, \quad (38)$$

where $D(q) = 1/G(q) = 4 - 2\cos q_x a - 2\cos q_y a$ is the Fourier transform of $-\Delta_\mu^2 = G^{-1}$. As we want to consider the long-range behavior of this equation, we take $D(q)_{q \rightarrow 0} \approx (qa)^2$, and then we have

$$\phi(q) = \frac{n(q)}{1 + (\tau_\theta / \tau_\Phi) [q^2 a^2 / \Lambda(q)]}. \quad (39)$$

In the case of local screening, as in model A, $\Lambda(q)$ is given by Eq. (31), and we get an effective Josephson penetration depth $\tilde{\lambda}_J = (\tau_\theta / \tau_\Phi \bar{\Lambda})^{1/2} a = \bar{\kappa}_J a$.

For model C, $\Lambda(q)$ is linear in q , Eq. (32), and then the penetration depth is $\lambda_p = (\tau_\theta / \tau_\Phi) a = \kappa_p a$, defining the parameter $\kappa_p = \lambda_p / a$. This is equivalent to Pearl's penetration depth for a thin film,²⁴ extended to a JJA.^{19,23}

B. Effective vortex-vortex interaction

In JJA's without screening it is known that the long-range interaction energy between vortices is logarithmic,^{1,4} which is the crucial ingredient in the BKT scenario.³ Let us see how the effective (i.e., long-range) interaction between vortices is affected by the SIMF effects.

This can be evaluated easily by mapping the Hamiltonian

$$\begin{aligned} \mathcal{H} = & E_J \sum_{r, \mu} \{1 - \cos[\Delta_\mu \theta(r) - A_\mu(r)]\} \\ & + \frac{1}{2} \sum_{R, R'} [\Phi(R) - \Phi_x] L^{-1}(R, R') [\Phi(R') - \Phi_x] \end{aligned} \quad (40)$$

to the Coulomb gas analog,

$$\begin{aligned} \mathcal{H}_{CG} = & 2\pi^2 E_J \sum_{R, R'} [n(R) - \phi(R)] G(R, R') [n(R') - \phi(R')] \\ & + 2\pi^2 E_J \kappa_p \sum_{R, R'} [\phi(R) - f] \Lambda^{-1}(R, R') [\phi(R') - f]. \end{aligned} \quad (41)$$

It is possible to get an effective vortex-vortex interaction by evaluating the partition function $\mathcal{Z} = \int d\{\theta(r)\} \int d\{\phi^i(R)\} e^{-\mathcal{H}_{CG}[\theta(r), \phi^i(R)] / kT}$, with $\phi^i(R) = \phi(R) - f$, and then doing the resulting Gaussian integral in $\phi^i(R)$.²³ Then the following effective Hamiltonian is obtained:

$$\mathcal{H}_{CG} = \sum_{R, R'} [n(R) - f] \mathcal{U}(R, R') [n(R') - f], \quad (42)$$

where $\mathcal{U}(R, R') = 2\pi^2 E_J U(R, R')$ is the effective interaction energy between two vortices located at R and R' , and $U(R, R')$ is the solution to

$$-\Delta_\mu^2 U(R, R') + \frac{1}{\kappa_p} \sum_{R''} \Lambda(R, R'') U(R'', R') = \delta_{R, R'}. \quad (43)$$

We should mention that in this Coulomb gas approach, the periodic pinning potential of the lattice has been neglected. This will be relevant in the strong screening case as we will see in the next section.

The dependence of $U(R, R') = U(R - R')$ for large R can be analyzed from the $q \rightarrow 0$ behavior of its Fourier transform,

$$U(q) = \sum_R e^{iq \cdot R} U(R) = \frac{1}{D(q) + \kappa_p^{-1} \Lambda(q)}. \quad (44)$$

For a short-range inductance matrix as in model B, we get, after using Eq. (31),

$$\mathcal{U}(R) = \frac{\pi E_J}{1 + \Lambda_2 / \kappa_p} K_0 \left(\frac{R}{\tilde{\lambda}_J} \right), \quad (45)$$

with $\tilde{\lambda}_J = [(\kappa_p + \Lambda_2) / \bar{\Lambda}]^{1/2} a$, and K_0 the modified Bessel function of the second kind. This has the limiting behavior

$$\begin{aligned} \mathcal{U}(R) = & \frac{\pi E_J}{1 + \Lambda_2 / \kappa_p} \left[\ln \frac{\tilde{\lambda}_J}{R} + \ln 2 - \gamma \right], \quad R \ll \tilde{\lambda}_J \\ \mathcal{U}(R) = & \frac{\pi E_J}{1 + \Lambda_2 / \kappa_p} \frac{e^{-R/\tilde{\lambda}_J}}{\sqrt{2\pi R/\tilde{\lambda}_J}}, \quad R \gg \tilde{\lambda}_J. \end{aligned} \quad (46)$$

This effective interaction is equivalent to the one that exists between vortices in continuous three-dimensional superconductors.⁴⁴ It is also the same that was used by Minnhagen as an approximation for the SIMF effects in the BKT transition within the Coulomb gas analogy.²²

In model C we get, after using Eq. (32),

$$\mathcal{U}(R) = \frac{\pi^2}{2} E_J \left[H_0 \left(\frac{R}{\lambda_p} \right) - Y_0 \left(\frac{R}{\lambda_p} \right) \right], \quad (47)$$

where $\lambda_p = \kappa_p a$, H_0 is the Struve function, and Y_0 is the Bessel function of the second kind. The limiting behaviors of this solution are

$$\mathcal{U}(R) = \pi E_J \left[\ln \frac{\lambda_p}{R} + \ln 2 - \gamma \right], \quad R \ll \lambda_p$$

$$\mathcal{U}(R) = \pi E_J \frac{\lambda_p}{R}, \quad R \gg \lambda_p. \quad (48)$$

This long-range vortex-vortex interaction energy has also been obtained by Stroud and Kivelson for arrays with screening.²³ It is equivalent to the interaction energy calculated by Pearl for two-dimensional superconductors.²⁴ Note that the main difference from (46), apart from a redefinition of the penetration depth, is the very slow decrease of the interaction energy for long distances ($1/R$ instead of exponential). This same difference was found in the numerical simulations of Phillips *et al.*²⁶

IV. MAGNETIC PROPERTIES

Here we study the magnetic response of IJJA's at $T=0$. We will show results obtained either with model A or with model C (the response with model B is essentially the same as in model A by replacing $\Lambda_0 \rightarrow \bar{\Lambda} = \Lambda_0 - 4\mathcal{M}$).

In this section we calculate the magnetization m as a function of field f , and the stationary vortex and field distributions for a given value of f . All the magnetization curves we show here were obtained starting from $f=0$ and $\phi(R, t=0)=0$, and then increasing f by δf steps taking as initial condition the final configuration of the previous step, i.e., $\phi(R, t=t_0, f+\delta f) = \phi(R, t=t_f, f)$. We also find essentially the same results taking as initial condition $\phi(R, t=0)=0$ for every f . Note that under these initial conditions, the magnetization does not have to be periodic in f (see Appendix A).

Our main result here is that there is a qualitative change of behavior when going from $\kappa \geq 1$ to $\kappa \leq 1$, where κ stands for either κ_J or κ_p , depending on which inductance matrix model we are using. This behavior change resembles the difference between hard and soft superconductivity in continuous superconductors. We name the two regimes type I and type II, respectively.

A. Type II regime

First we analyze the case which corresponds to a JJA with weak screening, i.e., $\kappa \geq 1$.

In Fig. 1(a) we show the magnetization m as function of f for model A with $\kappa_J=1.41$, and lattice size 30×30 . We note that for small fields m decreases linearly with f , and

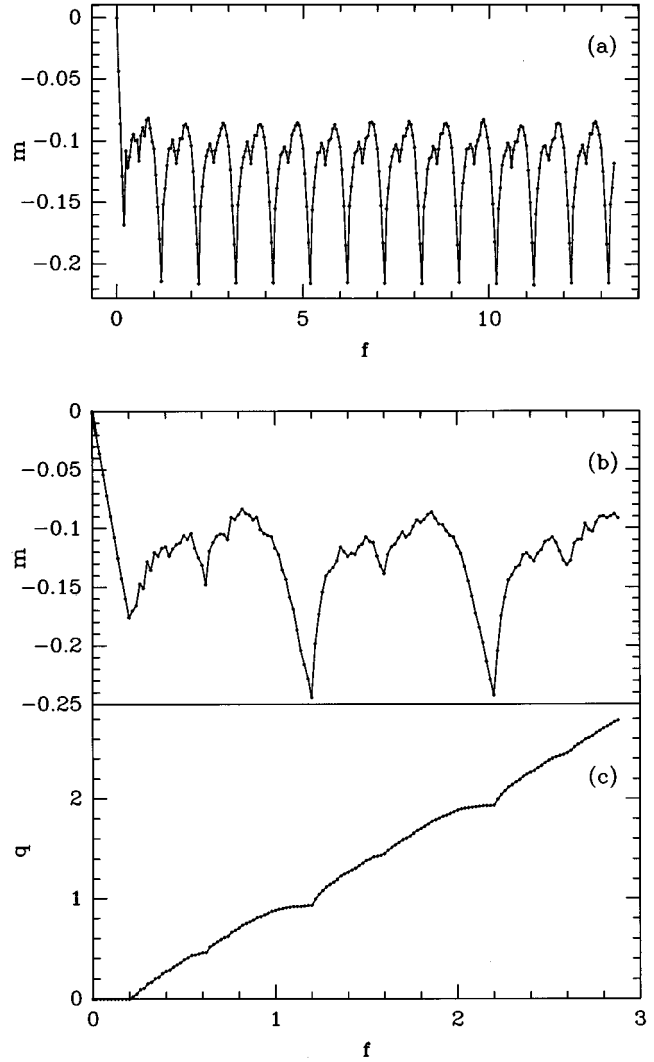


FIG. 1. (a) Magnetization m vs external magnetic field f for a 30×30 array with diagonal inductance matrix (model A) and $\kappa_J=1.41$. (b) The same as (a) but for a 40×40 array. (c) Vortex density q vs magnetic field f for the same array as in (b).

then for larger fields the curve shows oscillatory behavior with period $f=1$. This is consistent with the symmetries of the Hamiltonian (see Appendix A). In Fig. 1(b) we show the magnetization for small fields for the same κ_J in more detail while Fig. 1(c) shows the corresponding vortex density q for the same parameter values. We see that the linear decrease of m corresponds to a state without vortices, $q=0$, i.e., a Meissner-like state. Then above a critical field f_{c1} , vortices start to penetrate the array and the magnetization starts to oscillate. For fields $f > f_{c1}$, we note a structure in the curve that resembles that found in noninductive JJA's for fractional f .^{1,4,45} We see that close to fractional $f=r/s$, notably close to $f=n+1/2$, the magnetization starts to be quasilinear and q is almost constant, up to a certain $f=r/s + \delta f$, in which the magnetization has a minimum.

In Fig. 2 we show the magnetization curve for model C with $\kappa_p=2$, and lattice size 32×32 . In this case the calculations are more CPU intensive; thus we have fewer points than in Fig. 1. However, we essentially see a similar structure as in Fig. 1(b).

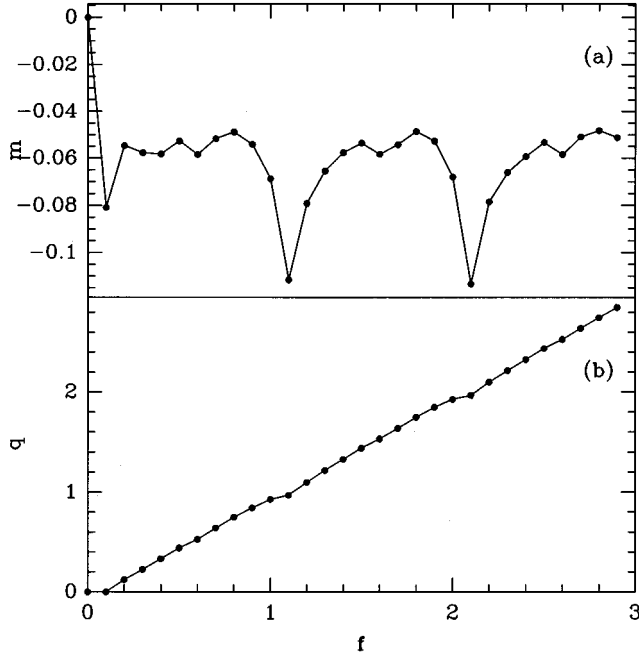


FIG. 2. (a) Magnetization m vs external magnetic field f for a 32×32 array with full inductance matrix (model C) and $\kappa_p = 2$. (b) Vortex density q vs magnetic field f for the same array as in (a).

Since in either case the magnetization never goes to zero, there is no upper critical field “ f_{c2} .” However, we define f_{c2} as the field for which $q=1$, i.e., for which there is one vortex everywhere, and we find that $f_{c2} \approx f_{c1} + 1$. In a sense this field represents the field above which the properties of the array repeat periodically with f .

For fields $f < f_{c1}$ the stationary state is a Meissner-like state. This is shown in Fig. 3(a) for model C with $\kappa_p = 2$. Similar results are obtained for model A. We find that the magnetic field decreases exponentially from the boundaries with a characteristic length that is approximately equal to $\kappa_p a$ in model C, or $\kappa_J a$ in model A.

Few vortices penetrate into the sample from the boundaries just above f_{c1} . In Fig. 3(b) we show the vortex distribution for $\kappa_J = 1.41$ for model A. As we will discuss later, this shows that f_{c1} actually corresponds to a critical field for vortex penetration through the boundaries, and not to the “equilibrium” critical field for nucleation of one vortex in the middle of the sample, which is lower (see Sec. IV E).

For larger fields, the vortices form structures in the array resembling the lattices found in the limit $\kappa = \infty$.⁴⁵ In Figs. 3(c) and 3(d) we show the vortex distributions for $f=1/2$ for model A with $\kappa_J = 1.41$, and for model C with $\kappa_p = 2$, respectively. We note that in both cases the vortex distributions have the same general structure. In both cases they have a crosslike symmetry, due to the finite size of the lattice, for it is easier for the field to penetrate from the corners. We see that the vortex distributions do not correspond to a perfect “checkerboard” as in the $\kappa = \infty$ case.⁴⁵ This is because now $q < f = 1/2$, for there is partial flux expulsion due to the finite penetration depth. These states correspond to flux penetration from the boundaries for they were obtained with initial condition $\phi(R, t=0) = 0$.

For larger fields, $f \gg f_{c1} + 1$, the vortex distributions $n(R)$ follow almost perfectly the symmetry transformation of $n(R) \rightarrow n(R) + p$ after $f \rightarrow f + p$, with p an integer.

The time needed to reach the stationary state also depends on f , as is shown in Fig. 4 for model A with $\kappa_J = 1.41$. Equilibrium is reached exponentially fast, in the Meissner state with a relaxation time of order τ_Φ ($f = 0.1 < f_{c1} = 0.21$ in the figure). For $f > f_{c1}$ much longer relaxation times are needed to form the vortex lattice starting from the initial condition $\phi(R, t=0) = 0$ ($f = 0.5$ in Fig. 4). In particular, close to f_{c1} the field penetration is very slow ($f = 0.22$ in the figure).

We have also analyzed the size dependence of the magnetization in this regime. Results are shown in Fig. 5, for model A with $\kappa_J = 1.41$. Here we see that f_{c1} is essentially size independent, and the magnetization tends to negatively increase with the size of the lattice. Note, however, that for smaller lattices the magnetization shows more structure while it becomes smoother for larger lattices. The reason for this is that the dips in m are related to vortex lattice commensurate states that fit inside the lattice. When the lattice is larger the number of rational numbers corresponding to commensurate vortex lattices increases but at the same time get to be closer in f so that for a fixed current mesh they essentially overlap and thus the smoother nature of m for larger lattices.

B. Type I regime

Below we show that the situation is very different when $\kappa \leq 1$ as compared to the type II regime discussed in the previous subsection.

Figure 6(a) shows the magnetization for model A, with $\kappa_J = 0.35$ for a lattice of 30×30 , and its corresponding vortex density is shown in Fig. 6(b). Again, for small fields m decreases linearly corresponding to a Meissner state with $q=0$. After a critical field $f_{c0} > 1$, vortices start penetrating the array. For larger fields the magnetization has a sawtooth-like behavior of period $f=1$, while the vortex density has a ladderlike structure, with plateaus and discontinuous jumps, also of period $f=1$.

In Figs. 7(a), and 7(b) we show the magnetization and vortex densities for model C with $\kappa_p = 0.1$. In this case the curves do not have the discontinuous jumps as in model A, but they do show a monotonic decrease and weak oscillatory behavior.

The similarities and differences between the two cases become more evident from looking at the vortex distributions. Below f_{c0} there is a Meissner state. This is shown in Fig. 8(a) for model C with $\kappa_p = 0.1$, the same as in model A. Again, the magnetic field decays exponentially with a characteristic length which is either $\kappa_p a$ or $\kappa_J a$ for each case. Just above $f_{c0} = 1.5$, we see that the vortices have penetrated the array in a very particular way, as shown in Fig. 8(b) for model A. They form a “vortex collar” all around the boundary, with constant vorticity $n(R = \text{boundary}) = 1$. In Fig. 8(c) we show the vortex distribution for much higher fields, $f \gg f_{c0}$. In this case, we see that the “collars” of constant vorticity have penetrated deeper into the array. The total vorticity of the collars decreases linearly from the boundary towards the center of the array. The linear slope with which the vorticity decreases is approximately equal to f_{c0} . In this high field regime, each time the field f is increased by 1, there is a collar vorticity increase from $n(R)$ to

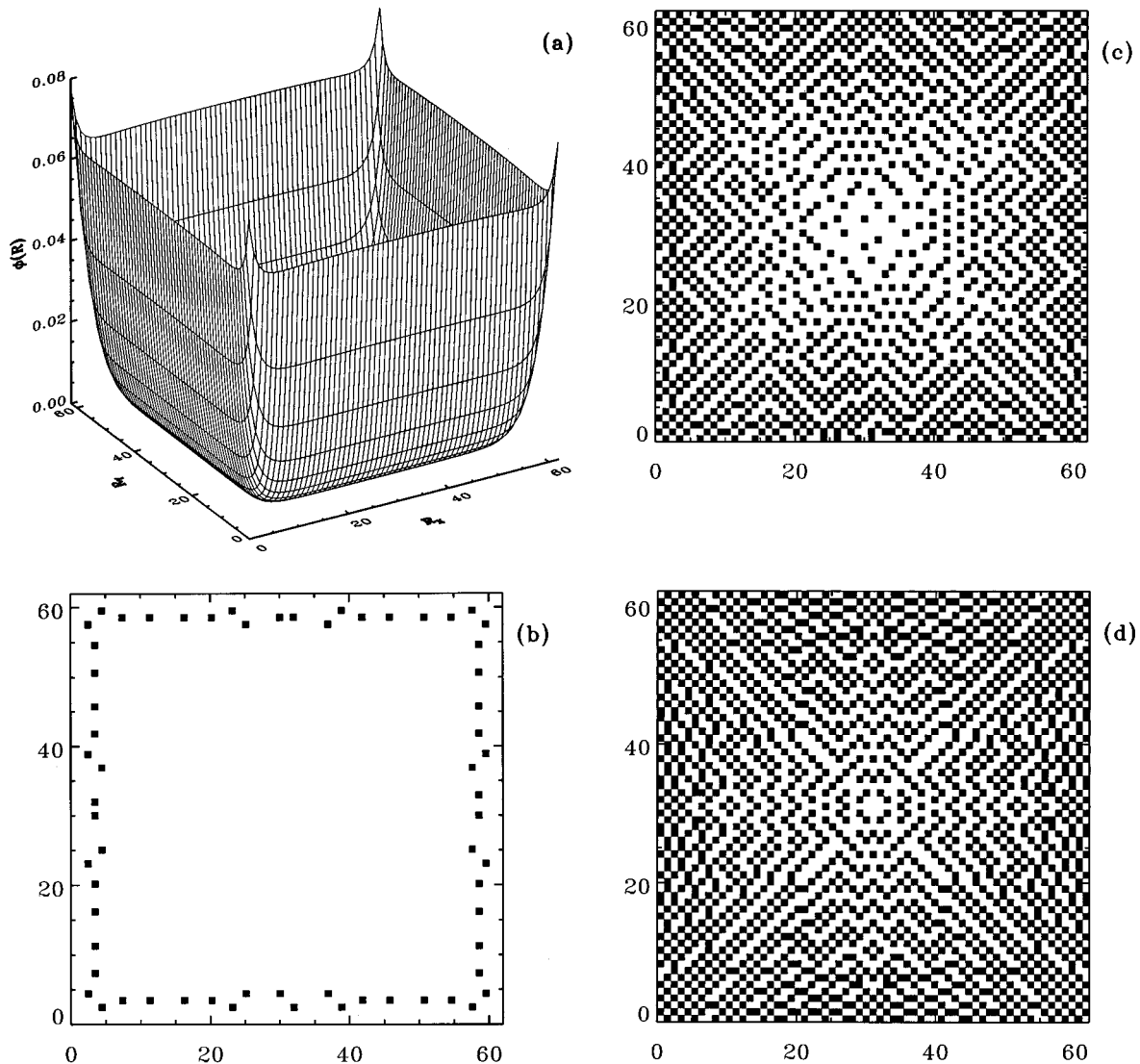


FIG. 3. (a) Magnetic flux distribution $\phi(R)$ showing the Meissner state for model C of an array with $\kappa_p=2$ for $f=0.1$. (b) Vortex distribution for a model A array with $\kappa_j=1.41$ and $f=0.22$, close to the critical field $f_{c1}=0.21$. Black squares represent vorticity $n(R)=1$. (c) Vortex structure for the same array as in (b) but for $f=0.5$. (d) Vortex structure for a model C array with $\kappa_p=2$ and $f=0.5$.

$n(R)+1$ in the whole array. This explains the jumps seen in the magnetization. Also, in Fig. 8(d) we show the vortex distribution for the model C and $f \gg f_{c0}$. We see again that in

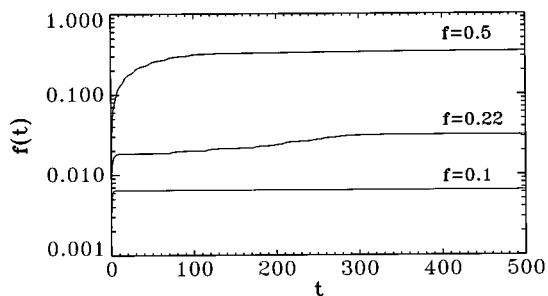


FIG. 4. Magnetic flux density as a function of time $f(t)$, for different fields $f=0.1$, $f=0.22$, and $f=0.5$; for a 64×64 array with diagonal inductance and $\kappa_j=1.41$. Here $f_{c1}=0.21$.

this case the vorticity decreases linearly from the boundaries towards the center of the array, with linear slope approximately equal to f_{c0} . The only qualitative difference is that the vorticity decrease shows more structure. Therefore the vorticity increases more smoothly when increasing the field, thus giving a magnetization that is smoother than in the diagonal case. We analyze the type I behavior in more detail below.

C. Effective attractive vortex interactions in type I regime

The fact that the vortex states and magnetization are essentially different in this regime compared to type II will become clearer after analyzing the interaction between vortices. A basic characteristic of these type I vortex states is that the vortices are all grouped together, instead of forming lattice structures as in the type II regime.

It is known that in continuous superconductors the vortex-vortex interactions are attractive in the type I case.⁴⁶ Let us

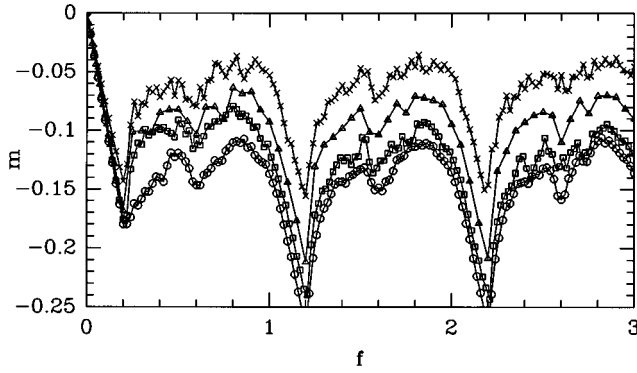


FIG. 5. Magnetization m vs magnetic field f for model A arrays with $\kappa_J=1.41$ for different lattice sizes. (\times) 16×16 , (Δ) 32×32 , (\square) 40×40 , (\circ) 48×48 .

then estimate the interaction energy of two neighboring vortices as compared to two well separated ones. The energy of two infinitely separated vortices is twice the energy of a single vortex. For an isolated vortex let us use the ‘‘arctan’’ approximation.¹⁹ In this case the phase differences around the plaquette for a vortex are all equal to $\Delta\theta = \pi/2$, and then the current flowing around the plaquette is $J = I_0 \sin \pi/2 = I_0$. The vortex energy is then $E_{1V} = 4E_J(1 - \cos \pi/2) + \frac{1}{2} L_0 I_0^2 = E_J(4 + \Lambda_0/2\kappa_p)$. Therefore the energy of two free vortices is approximately $E_{2V}^f = 2E_{1V} = E_J(8 + \Lambda_0/\kappa_p)$. For two nearest-neighbor bound vortices we approximate the phase difference in the junctions by $\Delta\theta = 2\pi/3$, except in the junction between them, for which $\Delta\theta = 0$. Then the mesh current in each one of the plaquettes will be $J = I_0 \sin 2\pi/3 = I_0 \sqrt{3}/2$, and the vortex energy for a pair is $E_{2V}^B = E_J(9 + \frac{3}{4}\Lambda_0/\kappa_p - \frac{3}{4}\mathcal{M}/\kappa_p)$. Therefore the energy difference $\Delta E_{2V} = E_{2V}^B - E_{2V}^f = E_J(1 - \frac{1}{4}\Lambda_0/\kappa_p - \frac{3}{4}\mathcal{M}/\kappa_p)$,

which can become negative for a characteristic $\kappa_p^* < (\Lambda_0 + 3\mathcal{M})/4 \approx 0.40$. For model A this condition reduces simply to $\kappa_J < 1/2$. Although this is a crude estimate it is important that it shows that below a characteristic κ_p^* the interaction between vortices will become attractive. Also note that this argument is independent of the long-range nature of the inductance matrix.

Another argument that shows how the effective interaction between vortices can become attractive follows from a ‘‘pinning’’ model. In Sec. III B we have calculated the vortex-vortex interaction energy $\mathcal{U}(R, R')$ in the Coulomb gas approximation. This energy is always repulsive but decreases as $\mathcal{U} \sim 2\pi^2 E_J \kappa_p$ in the high screening limit. However, in this approximation the lattice pinning potential has been neglected. If we consider the pinning potential energy, it increases with the magnetic screening, as has been calculated in Ref. 26. From this point of view we see that what is happening is that the vortices cannot overcome their repulsive ‘‘bare’’ interaction, for they are strongly pinned by the lattice. We can make this argument a bit more quantitative. In Fig. 9(a) we show the on-site $\mathcal{U}(R, R)$ bare interaction energy, calculated from Eq. (43), and the pinning energy barrier ΔE_P as a function of κ_p . {The pinning energy has been taken from the value estimated in Ref. 26, $\Delta E_P = 0.2E_J[1 + \frac{3}{2}(1/\kappa_p)(\Lambda_0 - \frac{8}{3}\mathcal{M})]$.} Also, in Fig. 9(b) we show the nearest-neighbor bare interaction energy $\mathcal{U}(R, R \pm \mu)$ compared with ΔE_P . In both cases we see that below a characteristic κ_p^* the pinning energy is larger than the interaction energy. We also see that the κ_p^* is essentially the same for either model C or B, while it is higher for model A. We also note that the κ_p^* for which $\Delta E_P = \mathcal{U}(R, R)$ ($\kappa_p^* \approx 0.14$ for models B and C, while $\kappa_p^* \approx 0.15$ for model A) is smaller than the κ_p^* for $\Delta E_P = \mathcal{U}(R, R \pm \mu)$ ($\kappa_p^* \approx 0.34$ for models B and C, and $\kappa_p^* \approx 0.5$ for model A). But

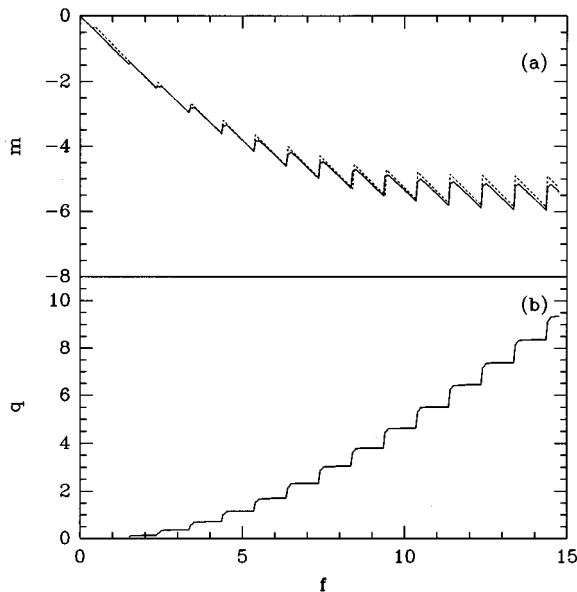


FIG. 6. (a) Magnetization m vs f , for a 30×30 array for model A with $\kappa_J=0.35$ (full line). The dashed line corresponds to the Bean model of Eq. (50) with $\alpha=1.0$. (b) Vortex density q vs f for the same parameter values as in (a).

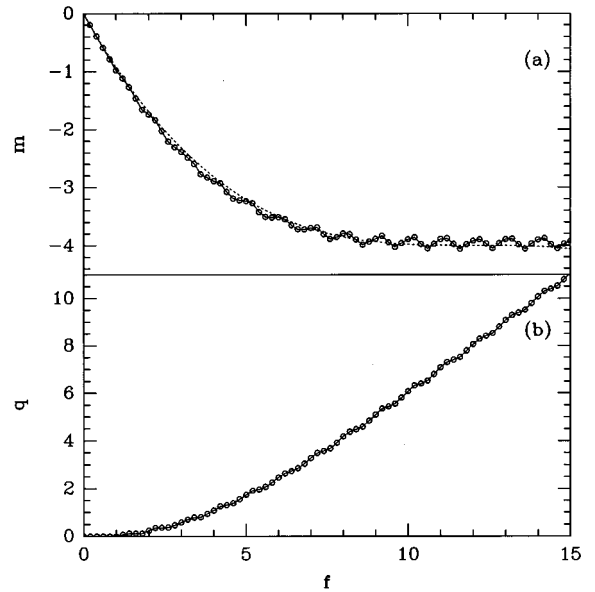


FIG. 7. (a) Magnetization m vs external magnetic field f for a 32×32 array for model C and $\kappa_p=0.1$ (full line). The dashed line corresponds to the Bean model result of Eq. (52) with $\alpha=0.75$. (b) Vortex density q vs f for the same parameter values as in (a).

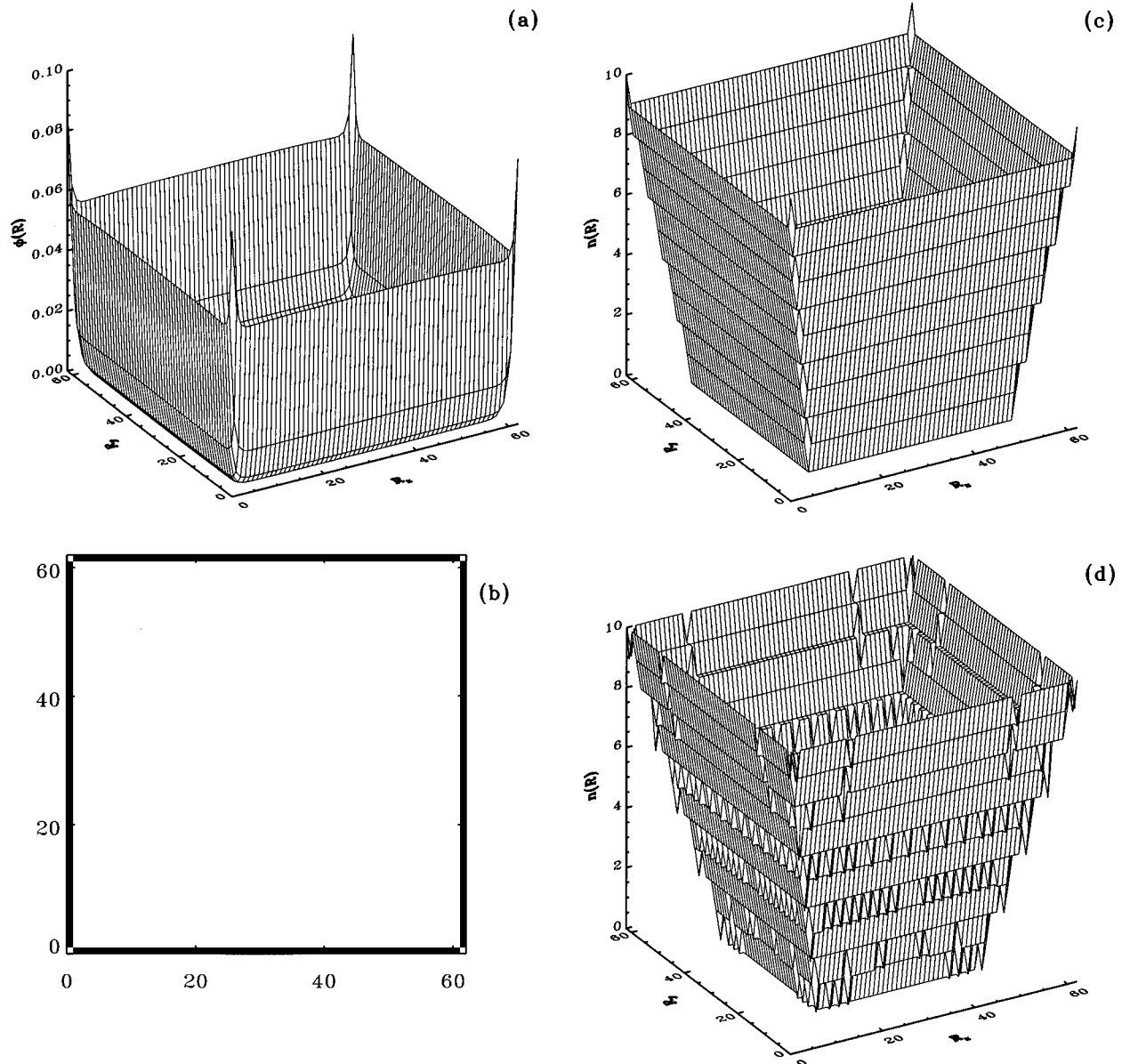


FIG. 8. (a) Magnetic flux distribution $\phi(R)$ showing the Meissner state for model C with $\kappa_p=0.1$ and $f=0.5$. (b) Vortex distribution for model A with $\kappa_J=0.35$ and $f=1.55$, slightly above the critical field $f_{c0}=1.5$. Black squares represent vorticity $n(R)=1$ and the corners are equal to zero. (c) Vortex distribution $n(R)$ for the same array as in (b) but for $f=10.3$. (d) The same as in (c) for a model C array with $\kappa_p=0.1$ and $f=10.3$.

in all cases $0.1 < \kappa_p < 1$. This means that when decreasing κ_p first the nearest-neighbor vortex interactions become attractive, and then at a lower κ_p the on-site interactions become attractive. This defines a crossover region between the type II and type I regimes as κ_p decreases. In our simulations we do not see a sharp transition from one regime to the other at a precise value of κ_p .

D. Bean model description

Since the type I regime can be thought of as a regime of “strong pinning,” a description similar to the Bean model⁴¹ for type II superconductors with strong pinning should be appropriate. In fact, the linear decrease of the magnetization shown in Figs. 8(c) and 8(d) can adequately be described by this model, as was suggested in Ref. 21.

Let us first discuss model A. In this case, just above f_{c0} the field penetrates as one collar around the boundary with constant vorticity $n(R)=1$. When increasing the field further, more vortex collars will penetrate the array in an ordered way. The average slope with which the vorticity decreases from collar to collar, when going towards the center, is about f_{c0} , i.e., f_{c0} measures how much the field has to be increased in order to get another collar inside. Let us compute how many vortices are in an array of size $N \times N$ for a given field f . The number of plaquettes in collar i is $4(N-2i+1)$, where i stands for the position of the collar from outside to inside ($i=1$ is the first collar close to the boundary). Then, if the vorticity of the $i=1$ collar is k , and it decreases with slope α , the vorticity of the collar i will be $k-\alpha(i-1)$. The total number of vortices in this case will then be

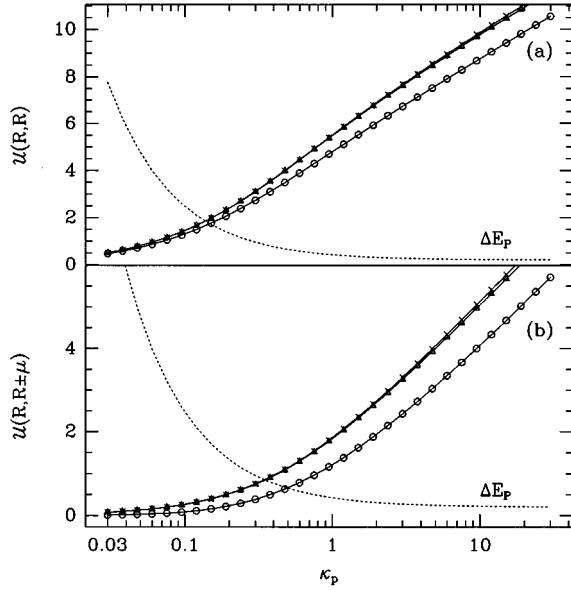


FIG. 9. (a) On-site bare interaction energy $\mathcal{U}(R,R)$ vs κ_p for model A (\circ), model B (\triangle), and model C (\times). The dashed line is the pinning energy barrier ΔE_p . (b) Nearest-neighbor bare interaction energy $\mathcal{U}(R,R\pm\mu)$ for the same cases as in (a).

$$Q = 4 \sum_{i=1}^{k/\alpha} [k - \alpha(i-1)](N - 2i + 1). \quad (49)$$

The magnetization is $m = Q/N^2 - f$, so that

$$m = \left(2 - \frac{2}{3N}\right) \frac{k}{N} + \left(1 - \frac{1}{N}\right) \frac{k^2}{k^*} - \frac{k^3}{3(k^*)^2} - f. \quad (50)$$

This is valid for $k < k^*$, where $k^* = (N/2)\alpha$, corresponding to the field for which the vortex collars have penetrated up to the center of the array. Now, k has to be close to f and jump by 1 when f is increased by 1. In Eq. (50) we take $k = [f - f_{c0}] + [f_{c0}]$, where $[x]$ = integer part of x . This gives for k^* an $f^* = (N/2)\alpha + f_{c0}$. At this field the array reaches its minimum magnetization

$$m^* = -f_{c0} - \alpha \left(\frac{N}{6} - \frac{1}{2} + \frac{1}{3N} \right). \quad (51)$$

Then for $f > f^*$ the vorticity is increased by 1 everywhere in the array each time f is increased by 1. In Fig. 6(a) we compare the numerically calculated magnetization with Eq. (50) for $\alpha \approx f_{c0}$. What is important from this ‘‘discrete’’ Bean model is that the magnetization is strongly size dependent, which is an important difference from the type II regime. This is shown in Fig. 10, for $\kappa_J = 0.35$. There we clearly see the size dependence of the magnetization and, in fact, m^* decreases linearly with N as given in Eq. (51).

We saw in Fig. 8(d) for model C that the field penetration was more complicated than in model A described by the vortex collars. But on average it also has a linear penetration with slope $\alpha \approx f_{c0}$. If we now assume a continuous version of the Bean model, i.e., vorticity decreasing linearly with slope α , we get the Bean model for the magnetization:

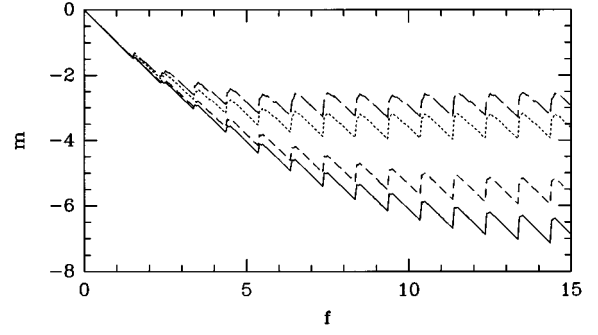


FIG. 10. Magnetization m vs f for model A arrays with $\kappa_J = 0.35$ and for different lattice sizes: 16×16 (long dashed line), 20×20 (dotted line), 30×30 (dashed line), and 40×40 (full line).

$$m = -f + \frac{f^2}{f^*} - \frac{1}{3} \frac{f^3}{(f^*)^2}, \quad f < f^* \quad (52)$$

$$m = -\frac{f^*}{3}, \quad f > f^*,$$

with $f^* = \alpha N/2$. In Fig. 7(a) we see that this functional dependence describes the overall calculated magnetization very well for the lattice size considered. Also, Eq. (52) can be used to describe the overall shape of the magnetization for model A, even when Eq. (50) is more accurate for a lattice system.

E. Critical fields

In Fig. 11 we show the calculated critical fields for vortex penetration in the array for model A as a function of κ_J . The critical fields were extracted from the magnetization curves and correspond to either f_{c1} or f_{c0} depending on which κ regime we are in.

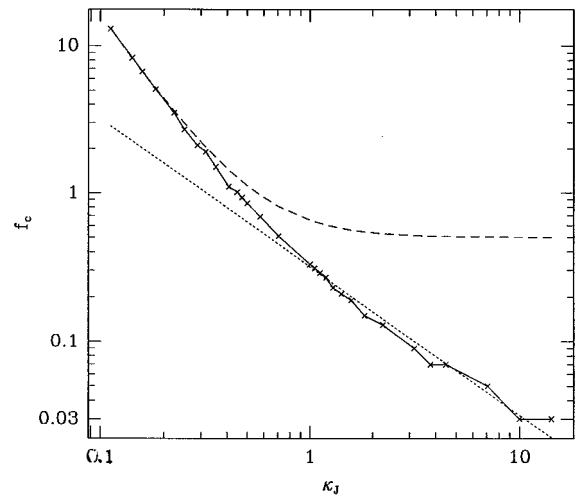


FIG. 11. Critical magnetic field f_c for vortex penetration for 30×30 arrays for model A as a function of κ_J . The dashed line corresponds to Eq. (60), and the dotted line corresponds to a fit with Eq. (62) with $\gamma = 6.119$ obtained from a fit to the data.

In order to interpret the data, we will analytically estimate the critical fields. Using the Coulomb gas approximation, the energy of the Meissner state can be calculated from Eq. (42) for $n(R)=0$,

$$E_M = 2\pi^2 E_J f^2 \sum_{R,R'} U(R,R'). \quad (53)$$

For large lattices we can neglect boundary effects and estimate $\sum_{R,R'} U(R,R') \approx \kappa_p N^2 / \bar{\Lambda}$ with $\bar{\Lambda} = \sum_R \Lambda(R,R')$, giving

$$E_M = 2\pi^2 E_J f^2 \frac{\kappa_p N^2}{\bar{\Lambda}}. \quad (54)$$

The energy corresponding to one vortex located at R_0 , $n(R) = \delta_{R,R_0}$, can be obtained from Eq. (42):

$$E_{1V} = 2\pi^2 E_J \left[U(R_0, R_0) - 2f \sum_R U(R_0, R) + f^2 \sum_{R,R'} U(R,R') \right]. \quad (55)$$

Then we can extract a critical field f_c for which $E_M = E_{1V}$ as

$$f_c = \frac{U(R_0, R_0)}{2 \sum_R U(R_0, R)}. \quad (56)$$

For a very large sample and R_0 away from the boundaries, this result is independent of R_0 . For example, if we approximate $U(R_0, R_0)$ by Eq. (48), and take $\sum_R U(R_0, R) \approx \kappa_p / \bar{\Lambda}$, we get

$$f_c \approx \frac{\bar{\Lambda}}{4\pi\kappa_p} \ln \kappa_p. \quad (57)$$

Note that since $\bar{\Lambda} \sim 1/N$ for $N \rightarrow \infty$, f_c is size dependent and $f_c \rightarrow 0$ for large N , analogous to what was found for two-dimensional superconducting films.^{24,47} The field f_c calculated this way corresponds to the vortex nucleation in the middle of the array. However, this is not the case considered in our calculations, since the critical fields we obtained for the magnetization correspond to the penetration from the boundaries. Let us estimate then the energy difference $\Delta E_{1V} = E_{1V} - E_M$,

$$\Delta E_{1V} = 2\pi^2 E_J \left[U(R_0, R_0) - 2f \sum_R U(R_0, R) \right]. \quad (58)$$

In Fig. 12 we show $\Delta E_{1V}(R_0, f)$ as a function of R_0 for different fields f . We see that when $f \sim f_c = 0.006904$ there is a potential barrier opposing vortex entry. After f is increased further, the barrier disappears and a vortex penetrates the array easily. In continuous superconductors this barrier has been calculated by de Gennes.⁴⁴ The critical field for which the barrier disappears corresponds to $(\partial \Delta E_{1V} / \partial R_0)_{R_0=a} = 0$, and is of the order of the thermodynamical critical field.⁴⁴

Let us estimate f_{c1} as the corresponding ‘‘thermodynamic critical field,’’ e.g., the field for which the energy of the

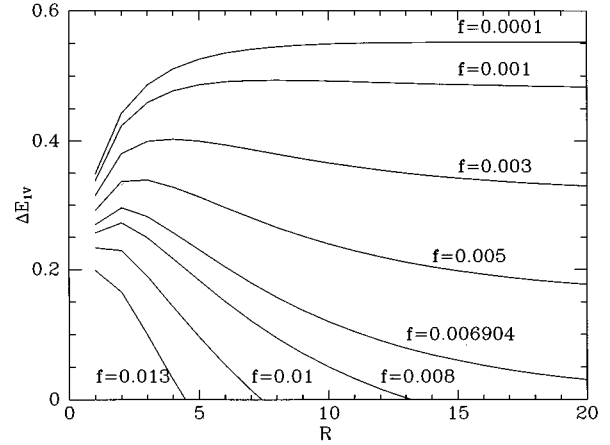


FIG. 12. Potential energy barrier for vortex penetration ΔE_{1V} as a function of f and $R_0 = (R_X, N/2)$ for an array of linear size $N=256$ and $\kappa_p=20$. Note that for the critical field estimated from Eq. (56), $f_c = 0.006904$, there is a potential barrier against vortex penetration from the boundary.

Meissner state equals the energy of the ‘‘normal’’ state. In the normal state there is no phase coherence, so $\langle \cos \Psi_\mu(r) \rangle = 0$, and $\phi(R) = f$; then

$$E_N = 2N^2 E_J. \quad (59)$$

After setting $E_N = E_M$, and using Eq. (54), we get

$$f_{c1} = \frac{1}{\pi} \left(\frac{\bar{\Lambda}}{\kappa_p} \right)^{1/2}, \quad (60)$$

which for model A is $f_{c1} = 1/\pi\kappa_J$. In Fig. 11 we see that this estimated f_{c1} fits the critical fields in the region $\kappa_J \gtrsim 1$ very well.

In the type I regime, $\kappa_J \lesssim 1$, the field penetration is different, as we saw before. The critical field corresponds to the penetration of a ‘‘collar’’ of vortices around the boundary, instead of a single vortex. Let us make a crude estimate of this critical field for model A. Take the kinetic energy as $E_K = E_J \sum_{r,\mu} [1 - \cos \Psi_\mu(r)]$, which is essentially proportional to the number of vortices in the collar, $4N$, so that $E_K \approx \gamma 4N E_J$, with γ a constant. For the magnetic part of the energy E_L , let us take $\phi(R) = 1$ for R in the collar, and $\phi(R) = 0$ otherwise. Then we get the energy of a collar, $E_{1C} = E_K + E_L$, as

$$E_{1C} \approx \gamma E_J 4N + \frac{2\pi^2 E_J \kappa_p}{\Lambda_0} [4N(1-f)^2 + (N^2 - 4N)f^2]. \quad (61)$$

After comparing with the Meissner state energy, Eq. (54), $E_{1C} = E_M$, we get

$$f_{c0} \approx \frac{1}{2} + \frac{\gamma}{4\pi^2} \frac{\Lambda_0}{\kappa_p} = \frac{1}{2} + \frac{\gamma}{4\pi^2} \kappa_J^{-1/2}. \quad (62)$$

In Fig. 11, we see that this expression for f_{c0} can fit the calculated critical fields in the small- κ_J regime, with $\gamma = 6.119$.

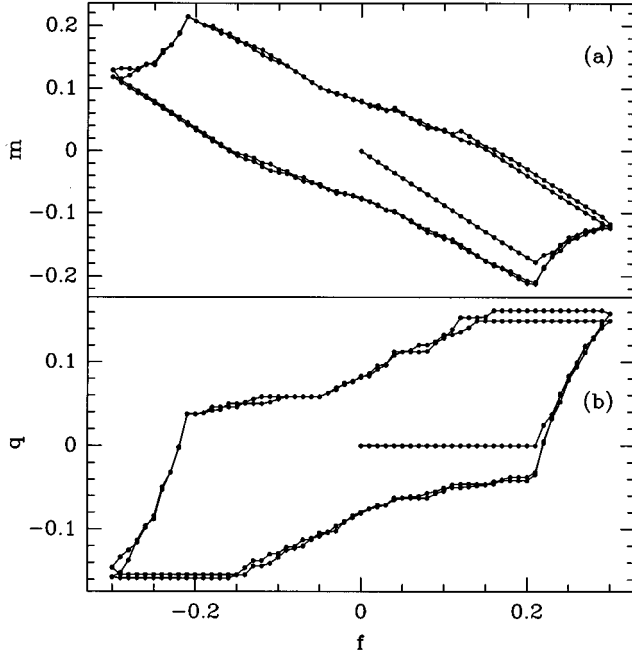


FIG. 13. Hysteresis loops in (a) the magnetization m and (b) the vortex density q as a function of f . Model A arrays of size 30×30 and $\kappa_J = 1.41$.

F. Hysteresis and remanent magnetization

The presence of pinning due to the lattice periodic potential makes the magnetic response history dependent. Here we show results for the magnetization for model A with increasing and decreasing external field f . The magnetization curves are obtained by incrementing the field by δf , and taking the final configuration for f as an initial condition for $f + \delta f$. We increase the field up to an f_{\max} starting from $f = 0$, and then decrease it down to $-f_{\max}$, then increase it again, repeating this cycle several times. We found that whenever we turn back the field for $f_{\max} < f_{c1}$ or $f_{\max} > f_{c0}$, depending on the value of κ_J , the magnetization curve is completely reversible. However, once there are vortices inside the array, reversibility is lost. In Fig. 13(a) we show the hysteresis loop in the magnetization when $f_{c1} < f_{\max} < 1 + f_{c1}$, for an array with $\kappa_J = 1.41$, in the type II regime. In Fig. 13(b) we show the hysteresis in the vortex density q . Here we see that when the field is reversed, q remains constant for a certain f range (approximately up to $\approx f_{\max} - f_{c1}$). This means that the vortices remain pinned in the lattice until the external field has been reduced sufficiently so that some of the vortices start to be expelled. This makes it possible to have positive magnetization in the array. In Fig. 14(a) we show the case when $f_{\max} > f_{c1} + 1$, for $\kappa_J = 1.41$, also in the type II regime. Here, the symmetries of the Hamiltonian, discussed in Appendix A as a function of f , become evident. In fact, the upper branch of the hysteresis cycle (positive magnetization) can be reproduced after the transformation $f \rightarrow n - f$ of the lower branch.

Finally in Fig. 14(b) we show the case for an array in the type I regime, with $\kappa_J = 0.35$. Here the hysteresis cycle is much bigger than in the previous case because pinning is dominant in this regime. Also, the size of the hysteresis cycle

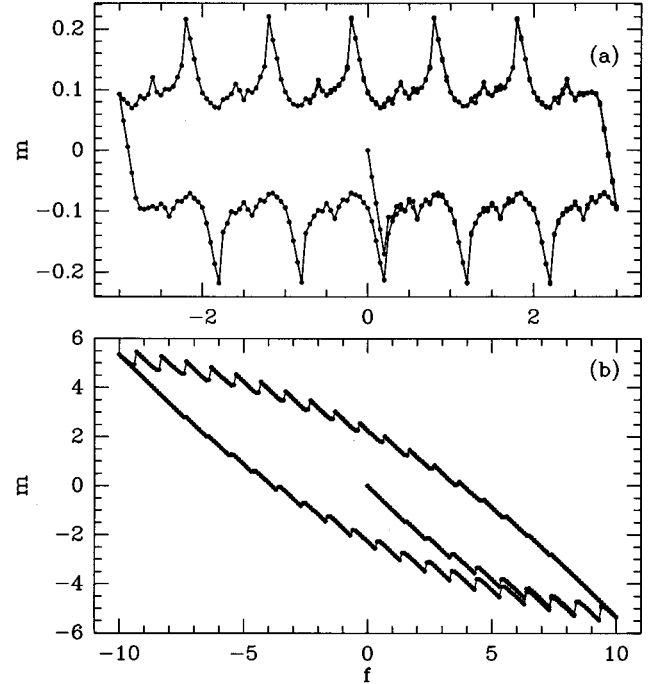


FIG. 14. Hysteresis loops in the magnetization m as a function of f for a model A 30×30 array. (a) $\kappa_J = 1.41$ and (b) $\kappa_J = 0.35$.

depends on the lattice size, as should have been expected from the Bean model's description of this regime.

We can also study the irreversible magnetic behavior of the IJJA by turning off the field after reaching the stationary state for a given f . In Figs. 15(a) and 15(b) we show the field profiles for $f = 0.3$ and $\kappa_J = 1.41$, before and after turning off the field, and in Figs. 15(c) and 15(d) for $f = 10.3$ and $\kappa_J = 0.35$. In both cases we see that there is a remanent magnetization in the array, since some vortices remain pinned by the lattice. In particular, in the type I regime the remanent field profile is also linear in R as could have been predicted within the Bean model description.

This magnetic irreversible behavior has also been noted by Majhofer *et al.*²¹ but not its connection with the presence of quantified vortices. Here we see that the irreversibility is due to the pinning of vortices in the lattice potential of the IJJA, and that in the type I like regime it can be described by a discrete version of the Bean model.

V. DC TRANSPORT PROPERTIES

In this section we study the IV characteristics of IJJA's when driven by a dc current. We pay particular attention to vortex distributions and the edge fields produced by the external current for models B and C. We also analyze the history-dependent properties of the IJJA as a function of κ .

A. Edge fields

When solving the dynamical IJJA equations with an external current I_{ext} one must carefully specify the boundary conditions. The reason is that total magnetic field, external + induced, depends on the external and internal currents (see

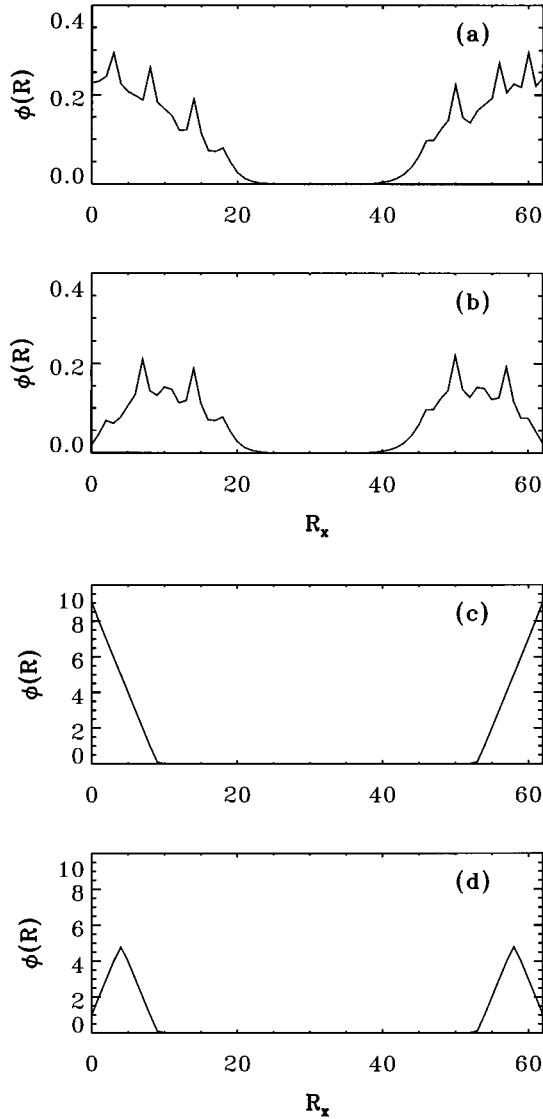


FIG. 15. Magnetic flux profiles in a model A 64×64 array. (a) For $\kappa_J = 1.41$ and $f = 0.3$. (b) The same as (a) but after turning off the field. (c) For $\kappa_J = 0.35$ and $f = 10.3$. (d) The same as (c) but after setting $f = 0$.

Appendix C for a detailed discussion of this point). The current conservation conditions are

$$\Delta_\mu \cdot I_\mu(r) = I_{\text{ext}}(r), \quad (63)$$

where $I_{\text{ext}}(r)$ depends on the boundary conditions. Here we take

$$\Delta_\mu \cdot I_\mu(r) = 0 \quad (64)$$

for all r and

$$\Delta_\mu \cdot I_\mu(r) = I_{\text{ext}} \quad (65)$$

for the top and bottom boundaries. From these current conservation conditions in the dual lattice we have

$$I_x(r, t) = J(R, t) - J(R - \hat{e}_y, t),$$

$$I_y(r, t) = J(R - \hat{e}_x, t) - J(R, t) + I_{\text{ext}}(t),$$

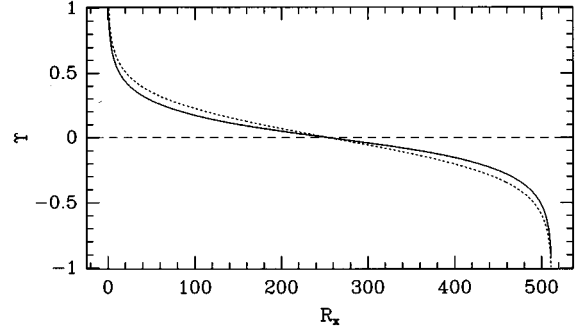


FIG. 16. Antisymmetric magnetic edge field distribution $E(R)$ for a 512×512 array along the direction perpendicular to the external current. The dotted line represents the approximation $E(R) \approx (\mu_0 a / 2\pi) \ln[(N_x a - R_x) / R_x]$.

where $J(R, t)$ is the plaquette's current. We can rewrite these equations as

$$I_\mu(r) = \Delta_\mu \times J(R) + \delta_{\mu, y} I_{\text{ext}}, \quad (66)$$

with the external current only applied along the y direction. In terms of the plaquette variables Eq. (5) the total flux is

$$\Phi(R, t) = \Phi_x(R) + \sum_{R'} L(R, R') J(R', t) + E(R) I_{\text{ext}}(t), \quad (67)$$

where

$$E(R) I_{\text{ext}}(t) = \sum_{r'} \Gamma(R, r', \hat{e}_y) I_{\text{ext}}(t). \quad (68)$$

This term gives the magnetic flux induced by the applied external currents, which is antisymmetric along the x direction. In Fig. 16 we show a plot of $E(R)$ along the x direction calculated within the filamentary approximation. These magnetic fields have maximum amplitude at the edges of the array and decrease towards its center, and thus they are called ‘‘edge magnetic fields.’’ For example, for a current sheet they are given by

$$E(R_x, R_y) \approx \frac{\mu_0 a}{2\pi} \ln\left(\frac{N_x a - R_x}{R_x}\right),$$

with $R_x \in [a, (N_x - 1)a]$. This result is a good approximation for the actual value of $E(R)$ (see Fig. 16). Note that the magnitude of E depends directly on the size of the array, and it decreases at the center of the lattice as the lattice size grows. In the limit $|N_x a / 2 - R_x| \ll N_x a$, $E(R_x) \approx (2\mu_0 / \pi N_x)(N_x a / 2 - R_x)$ at the center of the array. We note that there are other ways of separating and interpreting the different contributions in Eq. (6), as was done in Ref. 27.

We can now rewrite the normalized dynamical equations in the temporal gauge as

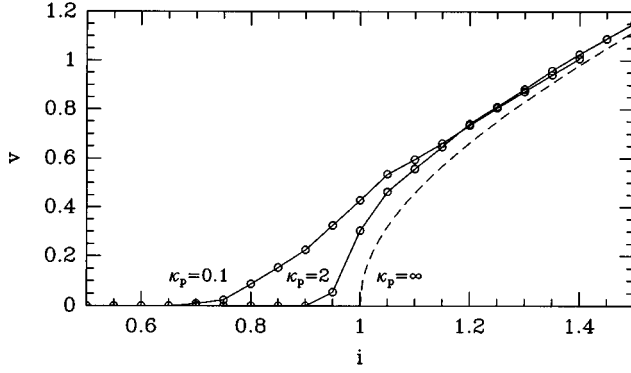


FIG. 17. Model C voltage-current characteristics for a 32×32 array for $f=0$. We show the extreme ($\kappa_p = \infty$) and moderate ($\kappa_p = 2$), type II regime and a type I regime ($\kappa_p = 0.1$) result.

$$\begin{aligned} \frac{d\Psi_\mu(r)}{dt} = & -\sin\Psi_\mu(r) - \kappa_p \Delta_\mu \times \sum_{R'} \Lambda^{-1}(R, R') \\ & \times \Delta_\mu \times \Psi_\mu(r') + 2\pi f + E(R')i/\kappa_p + \delta_{\mu, e_y} i, \end{aligned} \quad (69)$$

where we have normalized the edge fields, $E(R)/\mu_0 a \rightarrow E(R)$, and the external current, $i = I_{\text{ext}}/I_0$.

We note that in model A the edge fields are $E(R) = 0$ everywhere. The first approximation of the inductance matrix that takes the edge fields into account is in model B. In this case the matrix $E(R)$ reduces to $E(\text{left boundary}) = \mathcal{M}$, $E(\text{right boundary}) = -\mathcal{M}$, and $E(R) = 0$ elsewhere. Model C fully takes into account the edge fields as shown in Fig. 16.

The presence of antisymmetric magnetic edge fields has been identified as important in understanding the experiments by Lee *et al.* in Ref. 10. We have shown that even with model B the edge fields can produce subharmonic Shapiro steps as seen in the experiments.^{16,17}

B. IV characteristics and vortex states

Here we calculate the average voltage drop v along the current direction as defined in Eq. (30) as a function of the dc current i . This defines the IV characteristics of the IJJA. Reinel *et al.*²⁹ have also calculated IV curves of IJJA's. Here we complement the study of the IV curves with a calculation of the corresponding dynamical vortex states and the history dependence of the magnetic behavior of the IJJA.

When there is no external applied field, $f=0$, and for $\kappa = \infty$, it is known that the JJA dynamics at $T=0$ reduces to that of a set of uncoupled one-dimensional series arrays along the current direction.⁶ The IV characteristics can be reduced to that of a single Josephson junction, giving $v = \sqrt{i^2 - 1}$ for $i > 1$, and $v = 0$ for $i < 1$. If we neglect edge fields, the same is true for the IJJA for any value of κ , leading to IV characteristics independent of screening for $f=0$. As soon as the edge fields are included, in model B or C we find that the IV is different from that of a single junction case. We find that in the $f=0$ case there is a reduction of the IJJA critical current due to the presence of the edge fields, as is shown in Fig. 17. Note that this reduction is

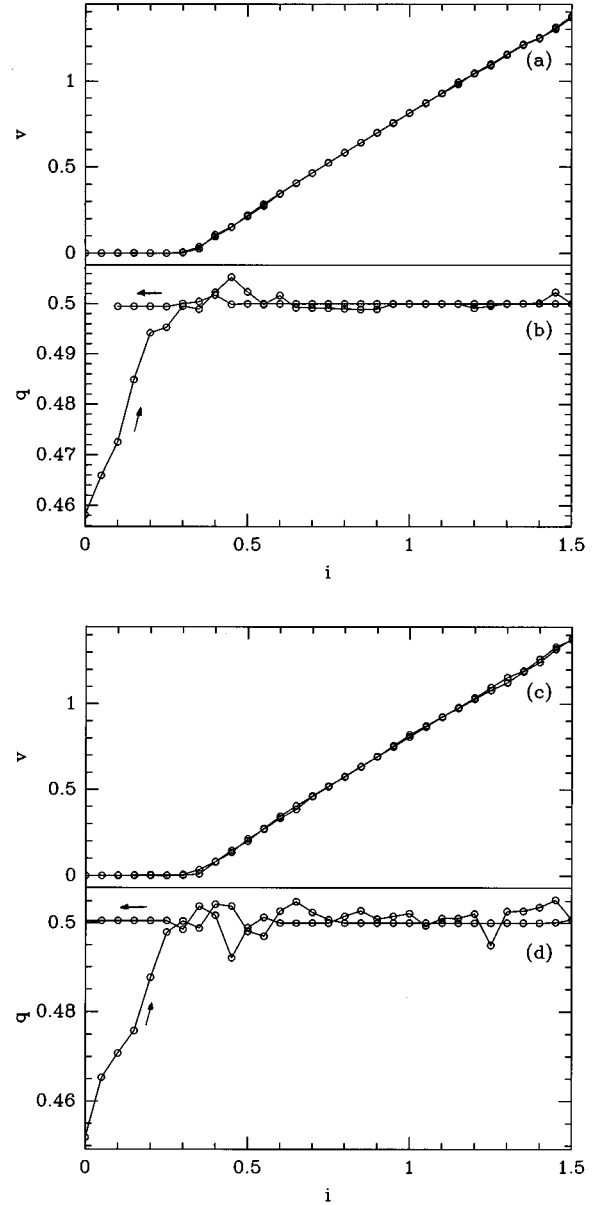


FIG. 18. (a) Voltage-current characteristics for model B for a 32×32 array and $\kappa_J = 1.41$ for $f = 0.5$. (b) Vortex density as a function of current for the same case as in (a). (c) Voltage-current characteristics for model C for a 32×32 array with $\kappa_p = 2$, for $f = 0.5$. (d) Vortex density as a function of current for the same parameters as in (c).

stronger in the type I regime. The dynamical vortex states that are induced by the edge fields in this case have been recently studied by Hagenaars *et al.*³⁰ They used the same model C as here, and their results compare very well with recent experiments by Lachenmann *et al.*³¹ measuring IV characteristics and images of vortex dynamics with a low-temperature scanning electron microscope (LTSEM) technique.

In Figs. 18(a) and 18(c) we show the IV characteristics for the interesting $f=1/2$ case for models B and C, respectively, starting from the checkerboard ground state, in the type II regime. In both cases the IV curves are reversible when increasing and decreasing the current. However, when

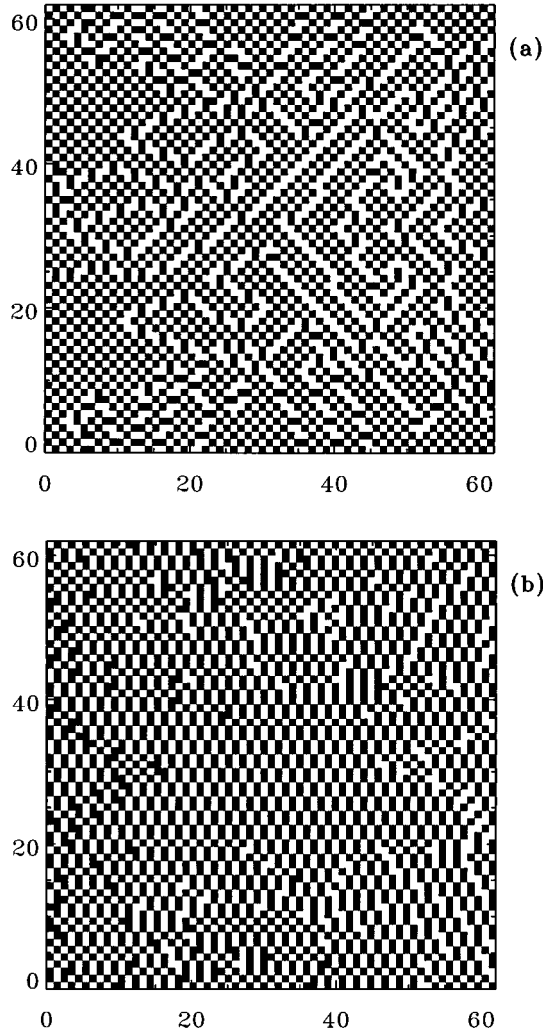


FIG. 19. Vortex structures for a model C array with $\kappa_p=2$ and $f=0.5$. Black squares represent vorticity $n(R)=1$, while for blank ones $n(r)=0$. (a) For a current $i=0.1$ ($i_c=0.27$); (b) for $i=1.5$.

we look at the corresponding vortex densities shown in Figs. 18(b) and 18(d), we find that they are history dependent. In both cases, at $i=0$, the vortex density is $q < f = 1/2$, as in the equilibrium state found in Sec. IV A. After turning on the current, q starts to increase and above the critical current i_c it reaches the value $q = 1/2$. For larger currents, in the “flux flow” regime, we always find that the vortex density stays around $q = f$. This regime corresponds to the region for which the IV curves are linear. When decreasing the current, the vortices stay pinned by the lattice below i_c , and the vortex density formed is maintained around $q = f$. Therefore the magnetic behavior of the array is irreversible even when the IV characteristics are reversible.

In Fig. 19(a) we show the vortex distribution for currents $i < i_c$ for model C (nearly the same kind of vortex distributions are seen for model B). This corresponds to the stationary state starting with zero vorticity as initial condition, i.e., to turning on the field only after the current is on. We note that the vortex distributions are different from the ones produced at $i=0$, even when the vortex density is approximately the same. Notice that there is a reflection symmetry along the

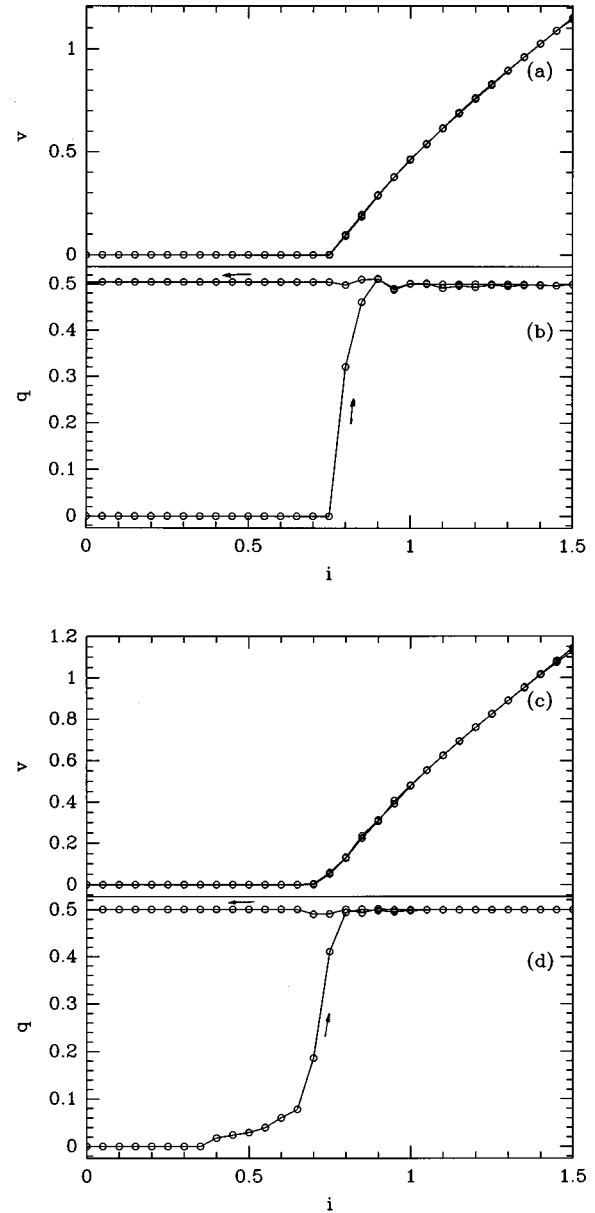


FIG. 20. (a) Voltage-current characteristics for model B for a 32×32 array with $\kappa_J=0.35$ and $f=0.5$. (b) Vortex density as a function of current for the same case as in (a). (c) Voltage-current characteristics for model C with a 32×32 array and $\kappa_p=0.1$ for $f=0.5$. (d) Vortex density as a function of current for the same parameter values as in (c).

current direction. But in the perpendicular direction the symmetry is broken by the Lorentz force caused by the current.

In the Ohmic regime above the critical current, $i \gg i_c$, the stationary moving vortex state has $q = f$ (and therefore zero magnetization). The vortex structure in this case does not correspond to the checkerboard pattern; it has a high density of domain walls and defects, as can be seen in Fig. 19(b). This situation is similar to the one seen in JJA’s without screening by Falo *et al.*⁷ for large currents.

In the type II regime, with high concentration of vortices, the edge field effects are very weak. In fact, we find nearly the same IV characteristics and the same kind of vortex structures when doing the simulations of model A.

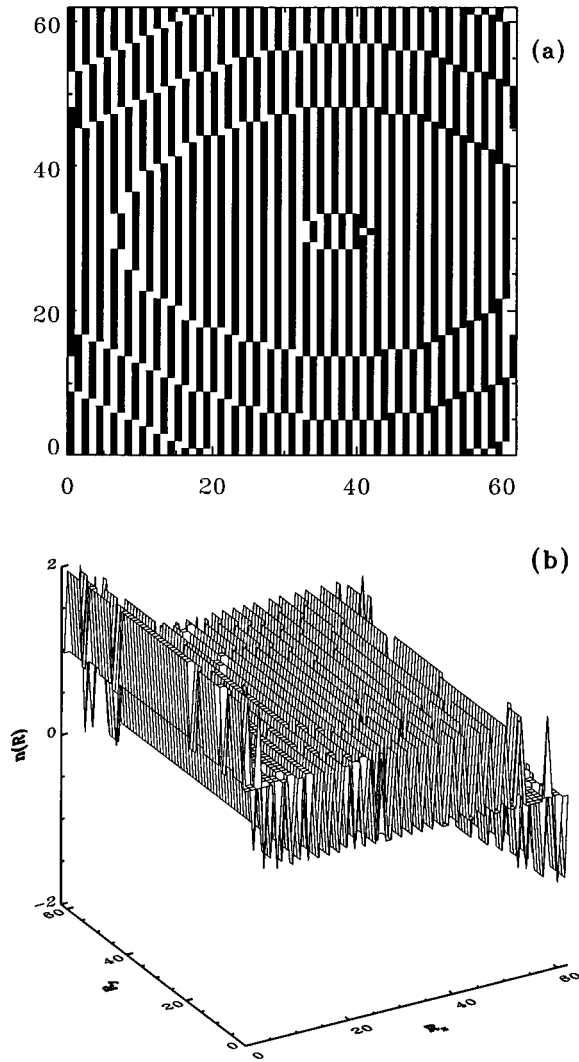


FIG. 21. (a) Vortex distributions for a model B array with $\kappa_p=0.5$ and $f=0.5$ and external current $i=1.5$. Black squares represent vorticity $n(R)=1$. (b) Surface plot of $n(R)$ for a model C array with $\kappa_p=0.1$, $f=0.5$, and $i=1.5$.

We now move on to discuss the type I regime. In Figs. 20(a) and 20(c) we show the IV curves for models B and C, respectively, for the same field, $f=1/2$. In this regime the critical current is much higher than in the type II regime. This is consistent with the fact that there is stronger pinning in this case. We show the vortex density as a function of currents in Figs. 20(b) and 20(d). Again, we find that the vortex densities formed are irreversible even when the IV 's are reversible while increasing and decreasing the current. The difference in this type I regime is that the initial state at $i=0$ is the Meissner state. When increasing the current, the array remains in the Meissner state ($q=0$). Then the vortices start to penetrate the array ($q \neq 0$) as the current approaches i_c from below. Finally, in the “flux flow” regime the vortex density equals the external field ($q=f$). Again, when decreasing the current from this state, vortices remain pinned inside the array below i_c , making its magnetic response history dependent.

It is interesting to see the vortex distribution in this case. This is shown in Fig. 21(a) for a current $i=1.5 > i_c$ for model

B. We note that the vortices are distributed in parallel “stripes” of constant vorticity along the external current direction. For this field we find alternating stripes of vorticity zero and 1, consistent with a vortex density of $q=0.5$. This state with stripes also has domain walls as can be seen in the figure. The stripes are due to the attractive vortex-vortex interaction in the type I regime, as shown in Sec. IV C. In particular, this vortex state is reminiscent of the intermediate state in type I superconductors, if we interpret the stripes of vorticity 1 as “normal” material. Note, however, that this state is dynamically generated by the driving current. See also that this vortex state corresponds to the one found to oscillate in the fractional giant Shapiro steps in the type I regime.^{16,17} We note that a similar dynamical vortex state was obtained in Ref. 28, in the row-switched state of an underdamped IJJA. In Fig. 21(b) we show the distribution of vorticity for the same case as above, but for model C. Here, the edge fields effect are strong and they affect the vorticity close to the boundaries. However, in the center of the array we see the same kind of vortex structure formed by stripes as seen in model B.

VI. DISCUSSION

Among the main results of this paper is that there is a qualitative change of behavior in the response of a JJA when going from weak to strong screening effects. This change is manifested in the magnetic and transport properties of IJJA's for both local and long-range inductances. This $\lambda \lesssim a$ regime loosely resembles that of type I superconductors in that the effective vortex interactions are attractive. Also, it can be thought of as a regime in which pinning dominates, and the magnetic behavior for high fields can be understood in terms of Bean's model. We note that even in superconducting quantum interference devices (SQUID's) there is a qualitative change in behavior when increasing the self-inductance \mathcal{L} such that $2\pi\mathcal{L}I_0/\Phi_0 > 1$.⁴⁸ In this case the change is from a reversible to an irreversible magnetic behavior. The IJJA's always show irreversibility in their magnetic response (as shown in Sec. IV F), since there is always a loop of radius R and inductance $\mathcal{L}_R \approx \mu_0 R$ such that $2\pi\mathcal{L}_R I_0/\Phi_0 > 1$ [in the case of model A, it should be $\mathcal{L}_R \approx L_0(R/a)^2$ instead]. Then the characteristic radius above which there is irreversible behavior is $R_c \approx \Phi_0/2\pi\mu_0 I_0 = \lambda_p$, and the crossover to type I behavior occurs for the smallest possible length scale, i.e., $R_c \approx a$.

We should mention that our magnetization studies have essentially considered vortex penetration from the boundaries. A different, and also interesting, problem to study is that of vortex nucleation inside the arrays. This, of course, will lead to different critical fields and magnetic responses, in particular in the $\lambda \lesssim a$ regime. We leave this issue for future studies.

From our results, it would seem at first sight that there are no significant differences between a local or the full inductance matrix approximations. There is in fact an important difference that relates to the long-range nature of the vortex-vortex interactions as already shown in Ref. 26. The difference was discussed in Sec. III B, and it is relevant at low vortex densities in the array ($q \ll 1$). It affects the quantitative value of the critical field for vortex nucleation as shown

by Phillips *et al.* It is not so important for the microscopic vortex configurations in which the vortex densities are high ($q \sim 1$), as was the case for the systems analyzed here.

In this paper we concentrated on the zero temperature regime. It will be interesting to study finite temperature effects in IJJA's by adding a Langevin current noise to Eq. (1). In particular, there is the question of stability against thermal fluctuations, in particular for $\lambda \leq a$. Our preliminary results show that this regime is stable.

ACKNOWLEDGMENTS

We acknowledge helpful discussions with J. Castro, F. de la Cruz, G. Chu, T. Hagenaaers, J. van Himbergen, and P. Tiesinga. This work has been partially supported by NSF Grant No. DMR-95-21845. D.D. acknowledges the International Centre for Theoretical Physics, Trieste, Italy, where part of this work was completed, for financial support.

APPENDIX A: HAMILTONIAN AND SYMMETRIES

The physical properties of JJA's without screening are invariant under the changes $f \rightarrow f+n$ and $f \rightarrow -f$, with $f = \Phi_x / \Phi_0$ and n an integer.⁴ These symmetries, which are manifestations of flux quantization in JJA's, have been widely tested experimentally.^{1,4}

The Hamiltonian for a JJA with screening, and without external currents, is

$$\begin{aligned} \mathcal{H} = E_J \sum_{r,\mu} & \left[1 - \cos(\Delta_\mu \theta(r) - A_\mu(r)) \right. \\ & \left. + \frac{1}{2} \sum_{R,R'} [\Phi(R) - \Phi_x] L^{-1}(R,R') [\Phi(R') - \Phi_x], \right] \end{aligned} \quad (\text{A1})$$

with $E_J = \Phi_0 I_0 / 2\pi$ the Josephson energy. It is not obvious that this Hamiltonian preserves these symmetries. We note that the ‘‘true’’ dynamical magnetic variable is the induced magnetic field and not the total field. We write $\Phi(R) = \Phi^i(R) + \Phi_x$ and $A_\mu(r) = A_\mu^i(r) + A_\mu^{\text{ext}}(r)$, with $\Phi^i(R)$ and $A_\mu^i(r)$ the induced flux and vector potential, respectively.

For example, in the Landau gauge the external vector potential $A_\mu^{\text{ext}}(r) = 2\pi f n_x \delta_{\mu, e_y}$, where $r = (n_x a, n_y a)$, and we get

$$\begin{aligned} \mathcal{H} = E_J \sum_r & \{ 2 - \cos[\Delta_x \theta(r) - A_x^i(r)] - \cos[\Delta_y \theta(r) - A_y^i(r)] \\ & - 2\pi f n_x \} + \frac{1}{2} \sum_{R,R'} \Phi^i(R) L^{-1}(R,R') \Phi^i(R'). \end{aligned} \quad (\text{A2})$$

It is now clear that the Hamiltonian is invariant under $f \rightarrow f+n$, but is not invariant under $f \rightarrow -f$, for the induced field changes sign, $\Phi^i(R) \rightarrow -\Phi^i(R)$. Therefore as soon as the dynamics of the magnetic field become important the ‘‘reflection’’ symmetry is broken.

When we consider the time evolution of the dynamical system, given either by Eqs. (12) and (14) or by Eq. (20), we have to take into account the symmetries of the initial con-

ditions. The solutions have the same response under a symmetry transformation $f \rightarrow f+n$ only if the initial conditions satisfy the same symmetry. For example, if we study the IJJA under a frustration f with initial condition $\Phi(R, t=0) = 0$ for all R we get the same physical response for a frustration $f+n$ after an initial condition $\Phi(R, t=0) = n\Phi_0$ for all R .

APPENDIX B: ALGORITHMS

In this appendix we sketch the algorithms we used to calculate the dynamical behavior of the inductive Josephson junction arrays.

The numerical integration of the dynamical equations requires taking into account the relevant time scales of the system, i.e., the relation $\kappa_p = \tau_\theta / \tau_\Phi$. In the regime $\kappa_p \gg 1$ the fast variables are the fluxes while the θ 's are slow, with the opposite in the $\kappa_p \ll 1$ regime. This situation is typical of ‘‘stiff’’ problems in ordinary differential equations, which are notoriously difficult to treat numerically and even analytically, for they lead to singular perturbations.^{49,50} On the other hand, since the equations of motion are gauge invariant we have used this symmetry to find the most appropriate gauge to solve the equations. It turns out that one specific gauge does not allow us to efficiently solve the problem for all values of κ_p . In the $\kappa_p \gg 1$ limit the stiffness problem is very difficult to overcome since $\tau_\Phi \rightarrow 0$ as $\kappa \rightarrow \infty$. In this case, a convenient gauge to choose is the Coulomb gauge, Eqs. (12) and (14), because the variables θ and Φ are almost separated. We have implemented an algorithm that works in this case. However, our discussion in this paper concentrates on the intermediate regime $0.1 \leq \kappa_p \leq 10$, where the stiffness problem is less severe. Within this parameter range it is more convenient to use the temporal gauge, Eq. (20), to efficiently solve the problem. In this gauge, we used a fourth order Runge-Kutta algorithm to integrate the dynamical equations. Typical integration time steps were $\Delta t / \tau_{\min} = 0.02 - 0.1$ with $\tau_{\min} = \min(\tau_\theta, \tau_\Phi)$.

The second step is to efficiently evaluate the right hand side of Eq. (20). Let us first write these equations in a dimensionless form. We normalize the currents by I_0 , $I \rightarrow I/I_0$, time by τ_θ , $t \rightarrow t/\tau_\theta$, inductance by $\mu_0 a$, $\Lambda = L/\mu_0 a$, and fluxes by Φ_0 , $f = \Phi_x / \Phi_0$. Then Eq. (20) reads

$$\begin{aligned} \frac{d\Psi_\mu(r)}{dt} = & -\sin\Psi_\mu(r) - \kappa_p \Delta_\mu \\ & \times \sum_{R'} \Lambda^{-1}(R,R') [\Delta_\mu \Psi_\mu(r') + 2\pi f]. \end{aligned} \quad (\text{B1})$$

We studied this dynamical system in square arrays of size $N \times N$ with free boundary conditions. We solved Eq. (B1) in two steps.

The first step consists of obtaining the mesh currents $J(R)$ from $\Psi_\mu(r)$, solving the equation

$$\sum_{R'} \Lambda(R,R') J(R') = -\kappa_p [2\pi f + \Delta_\mu \times \Psi_\mu(r)], \quad (\text{B2})$$

which can be simply written in matrix notation as

$$\mathbf{\Lambda}\mathbf{J}=\mathbf{\Phi}. \quad (\text{B3})$$

This step is the crucial part of the algorithm, and it depends on the specific model for the inductance matrix.

For model A we directly evaluate

$$J(R)=-\frac{\kappa_p}{\Lambda_0}[2\pi f+\Delta_\mu\times\Psi_\mu(r)]. \quad (\text{B4})$$

For model B, one has to solve for $J(R)$ from

$$\Lambda_0 J(R)-\mathcal{M}\sum_{\mu} J(R\pm\mu)=-\kappa_p[2\pi f+\Delta_\mu\times\Psi_\mu(r)], \quad (\text{B5})$$

or

$$\mathbf{\Lambda}_{\text{NN}}\mathbf{J}=\mathbf{\Phi}. \quad (\text{B6})$$

We solve this equation by performing a fast sine transform (the Fourier transform consistent with the boundary conditions) in the x direction and then solving the resulting tridiagonal equation along the y direction. This is in the same spirit as the FACR (Fourier analysis and cyclic reduction) algorithm, typically used as a fast solver for the Poisson equation.^{49,51} The computing time needed for each fast sine transform is on the order $N\ln N$ and solving each tridiagonal matrix is on the order of N ; therefore the total computing time varies as $N^2\ln N$.

It is more complicated to solve model C. There we have to solve (B2) for a matrix $\mathbf{\Lambda}$ where all the N^4 elements have to be considered. In this case we use an algorithm like the one introduced by Phillips *et al.*²⁶ It consists of noting that $\Lambda(R,R')=\Lambda(R-R')$, so that we can do the matrix product with $J(R)$ using the fast Fourier transform (FFT). We have to pad $J(R)$ and $\Lambda(R)$ with zeros because of the finite boundary conditions in order to adequately use the FFT technique, thus doubling their linear dimensions to $2N$. Being able to do this matrix multiplication very fast makes it appropriate to solve (B2) via an iterative method, like the ones used to solve linear sparse matrices.^{49,52} We use the conjugate gradient method,⁴⁹ preconditioned⁵² by the nearest-neighbor matrix $\mathbf{\Lambda}_{\text{NN}}$. This means that instead of solving for \mathbf{J} in $\mathbf{\Phi}=\mathbf{\Lambda}\mathbf{J}$, we solve for $\mathbf{Y}=\mathbf{\Lambda}_{\text{NN}}\mathbf{J}$ in $\mathbf{\Phi}=\mathbf{\Lambda}\mathbf{\Lambda}_{\text{NN}}^{-1}\mathbf{Y}$. The CPU time involved in this calculation varies as $k(2N)^2\ln(2N)$, with k the number of iterations needed by the conjugate gradient method to converge. Typically, we needed $k=10$ to solve the system with double precision floating point arithmetic.

After obtaining $J(R)$ the last step is simply to evaluate

$$\frac{d\Psi_\mu(r)}{dt}=-\sin\Psi_\mu(r)+\Delta_\mu\times J(R) \quad (\text{B7})$$

directly.

APPENDIX C: BOUNDARY CONDITIONS

There is an ambiguity in the definition of the mesh currents $J(\mathbf{R})$. In model C this ambiguity is irrelevant, since any choice of $J(\mathbf{R})$ leads to the same physical result. However, this ambiguity turns out to be relevant for the boundary con-

ditions of models A and B. In the recent literature^{27,16} the ‘‘self-inductance approximation’’ has led to different results. We show below that this difference arises from different definitions of $J(\mathbf{R})$ and its boundary conditions.

The physically well defined quantity is the current flowing in the junctions, $I_\mu(\mathbf{r})$. Current conservation states that

$$\Delta_\mu\cdot I_\mu(\mathbf{r})=0, \quad (\text{C1})$$

except at the top and bottom boundaries, where

$$\Delta_\mu\cdot I_\mu(\mathbf{r})=I_{\text{ext}}. \quad (\text{C2})$$

One possible choice for $J(\mathbf{R})$, let us call it choice (i), which satisfies these equations is

$$I_\mu(\mathbf{r})=\Delta_\mu\times J(\mathbf{R})+\delta_{\mu,e_y}I_{\text{ext}}, \quad (\text{C3})$$

with the boundary condition

$$J(\mathbf{R})=0, \quad (\text{C4})$$

for \mathbf{R} outside the array. Choice (i) is the one that we have used in our previous work in inductive JJA’s (Refs. 16 and 17) and in this paper. (It has also been used by Eikmans and van Himbergen in noninductive JJA’s.¹⁴)

Another possible choice, choice (ii), which also satisfies current conservation, is

$$I_\mu(\mathbf{r})=\Delta_\mu\times J(\mathbf{R}), \quad (\text{C5})$$

with the boundary conditions

$$J(R_x,0)=I_{\text{ext}}\left(\frac{N_x}{2}-R_x\right), \quad (\text{C6})$$

$$J(R_x,N_y)=I_{\text{ext}}\left(\frac{N_x}{2}-R_x\right),$$

$$J(0,R_y)=I_{\text{ext}}\frac{N_x}{2},$$

$$J(N_x,R_y)=-I_{\text{ext}}\frac{N_x}{2}.$$

Clearly, since these two $J(\mathbf{R})$ ’s are different they will induce different magnetic flux distributions. Let us consider the magnetic flux induced by the branch currents $I_\mu(\mathbf{r})$,

$$\Phi(\mathbf{R})=\Phi_x+\sum_{\mathbf{r}',\mu'}\Gamma(\mathbf{R},\mathbf{r}',\mu')I_{\mu'}(\mathbf{r}'). \quad (\text{C7})$$

We have for choice (i)

$$\Phi(\mathbf{R})=\Phi_x+\sum_{\mathbf{R}'}L(\mathbf{R},\mathbf{R}')J(\mathbf{R}')+I_{\text{ext}}E(\mathbf{R}), \quad (\text{C8})$$

with $L(\mathbf{R},\mathbf{R}')=\Delta_{\mu'}\times\Gamma(\mathbf{R},\mathbf{r}',\mu')$ and $E(\mathbf{R})=\sum_{\mathbf{r}'}\Gamma(\mathbf{R},\mathbf{r}',e_y)$. Note that the first term in this equation does not depend on the boundaries, since there we have $J(\mathbf{R})=0$, while the second term gives the magnetic field induced by the external currents (antisymmetric edge fields). In

this case, any truncation of the inductance matrix affects both $L(\mathbf{R}, \mathbf{R}')$ and $E(\mathbf{R})$ as discussed in the body of the paper.

For choice (ii) we have

$$\Phi(\mathbf{R}) = \Phi_x + \sum_{\mathbf{R}'} L(\mathbf{R}, \mathbf{R}') J(\mathbf{R}'). \quad (\text{C9})$$

Here the external currents are considered only on the boundary conditions for $J(\mathbf{R}')$. In this case a model A' gives only $L(\mathbf{R}, \mathbf{R}') = L_0 \delta_{\mathbf{R}, \mathbf{R}'}$, and model B' gives $L(\mathbf{R}, \mathbf{R}') = L_0 \delta_{\mathbf{R}, \mathbf{R}'} - M \delta_{\mathbf{R}, \mathbf{R}'}$. However, note that now the boundary condition on $J(\mathbf{R})$ for model A' gives a magnetic flux of $\Phi(\text{boundaries}) = \pm L_0 I_{\text{ext}} N_x / 2$ in the left and right boundaries. This must be compared with the absence of edge fields [$E(\mathbf{R}) = 0$] in model A with choice (i). Similar considerations lead to big differences between fields at the boundaries in models B and B'. But when considering model C, both choices (i) and (ii) become equivalent. The magnetic flux induced by $J(\mathbf{R})$ at the boundaries extends all over the sample and is equivalent to the edge magnetic fields.

In Fig. 22 we show the computed branch currents $I_\mu(\mathbf{r})$ for models A, B, and C for choices (i) and (ii) with a small bias current ($I_{\text{ext}} = 0.1I_0$) and $f = 0$. We take the current cross section along the direction of the applied current ($\mu = e_y$) at the middle of the array [$\mathbf{r} = (r_x, N_y a / 2)$]. Figure 22(a) shows the current distributions of choice (i) for models A, B, and C. We note that model A gives a completely uniform current distribution which is equal to the external current [$I_y(\mathbf{r}) = I_{\text{ext}}$]. For model C, part of the current accumulates close to the boundaries due to the edge magnetic fields, and the current tends to be homogeneous at the center of the array. Model B gives similar current distributions as model C, but with a smaller current concentrations at the edges, due to the weaker edge field effects in this model. The main difference between the three models appears only at the edges of the array, as shown in detail in the inset of Fig. 22(a). In Fig. 22(b) we show the current distributions for choice (ii) and models A, B, and C. Here we clearly see a significant difference for the truncated models as compared to choice (i). Models A' and B' give current distributions which are rather large at the edges and then fall off very

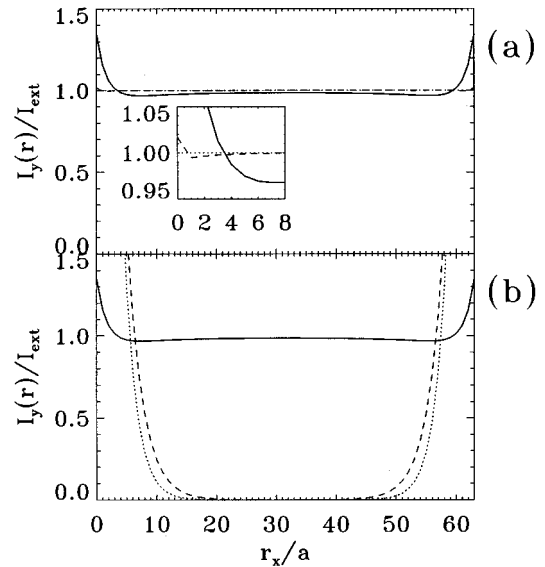


FIG. 22. Distribution of branch currents in a cross section perpendicular to the applied current in a 64×64 array. The applied current is $I_{\text{ext}} = 0.1I_0$ and $f = 0$. (a) For choice (i) of the mesh currents, solid curve: model C ($\kappa_p = 2$); dotted curve: model A ($\kappa_j = 2$); dashed curve: model B ($\kappa_j = 2$). The inset shows the current distributions close to the edges of the array. The apparent discontinuity in the dashed line is a numerical artifact due to the amplification and the size of the current mesh. (b) For choice (ii) of the mesh currents, solid curve: model C ($\kappa_p = 2$); dotted curve: model A' ($\kappa_j = 2$); dashed curve: model B' ($\kappa_j = 2$).

rapidly inside the array. The only difference between models A' and B' is in the decay range of the currents from the edges. Choice (ii) was used by Phillips *et al.*²⁷ when discussing the effects of truncating the inductance matrix in current-driven arrays and they obtained similar current distributions as shown in Fig. 22(b). As seen from Fig. 22(b), in this case there are very strong differences between models C and A' and B'. Instead, we have preferred to use choice (i), since models A and B give a much better approximation to model C, as is clear from Fig. 22(a).

*Present address: Centro Atomico Bariloche, 8400 S.C. Bariloche, Rio Negro, Argentina.

¹For a series of related papers, see *Physica B (Amsterdam)* **152**, 1 (1988).

²For recent reviews, see *Proceedings of the 2nd CTP Workshop on Statistical Physics: KT Transition and Superconducting Arrays*, edited by D. Kim *et al.* (Min Eum Sa, Seoul, Korea, 1993).

³J. M. Kosterlitz and D. J. Thouless, *J. Phys. C* **6**, 1181 (1973); V. L. Berezinskii, *Zh. Éksp. Teor. Fiz.* **61**, 1144 (1971); *ibid.* **59**, 907 (1970) [*Sov. Phys. JETP* **34**, 610 (1971); *ibid.* **32**, 493 (1970)].

⁴See, for example, C. D. Lobb, *Physica C (Amsterdam)* **126**, 319 (1989), and references therein.

⁵S. R. Shenoy, *J. Phys. C* **18**, 1543 (1985); **18**, 5163 (1985); R. Mehrotra and S. R. Shenoy, *Europhys. Lett.* **9**, 11 (1989).

⁶J. S. Chung, K. H. Lee, and D. Stroud, *Phys. Rev. B* **40**, 6570 (1989); K. K. Mon and S. Teitel, *Phys. Rev. Lett.* **62**, 673

(1989); W. Xia and P. L. Leath, *ibid.* **63**, 1428 (1989); P. L. Leath and W. Xia, *Phys. Rev. B* **44**, 9619 (1991); D. Domínguez, *Phys. Rev. Lett.* **72**, 3096 (1994).

⁷F. Faló, A. R. Bishop, and P. S. Lomdahl, *Phys. Rev. B* **41**, 10 983 (1990); N. Gronbech-Jensen, A. R. Bishop, F. Faló, and P. S. Lomdahl, *ibid.* **46**, 11 149 (1992).

⁸D. E. McCumber, *J. Appl. Phys.* **39**, 3113 (1968); W. C. Stewart, *Appl. Phys. Lett.* **10**, 277 (1968).

⁹S. P. Benz, M. S. Rzchowski, M. Tinkham, and C. J. Lobb, *Phys. Rev. Lett.* **64**, 693 (1990).

¹⁰H. C. Lee, D. B. Mast, R. S. Newrock, L. Bortner, K. Brown, F. P. Esposito, D. C. Harris, and J. C. Garland, *Physica B* **165&166**, 1571 (1990); H. C. Lee, R. S. Newrock, D. B. Mast, S. E. Hebboul, J. C. Garland, and C. J. Lobb, *Phys. Rev. B* **44**, 921 (1991); S. E. Hebboul and J. C. Garland, *ibid.* **43**, 13 703 (1991).

¹¹S. P. Benz and C. J. Burroughs, *Appl. Phys. Lett.* **58**, 2162 (1991).

- ¹²K. H. Lee, D. Stroud, and J. S. Chung, Phys. Rev. Lett. **64**, 692 (1990); K. H. Lee and D. Stroud, Phys. Rev. B **43**, 5280 (1991); J. U. Free, S. P. Benz, M. S. Rzchowski, M. Tinkham, C. J. Lobb, and M. Octavio, *ibid.* **41**, 7267 (1990); M. Octavio, J. U. Free, S. P. Benz, R. S. Newrock, D. B. Mast, and C. J. Lobb, *ibid.* **44**, 4601 (1991).
- ¹³M. Kvale and S. E. Hebboul, Phys. Rev. B **43**, 3720 (1991); M. S. Rzchowski, L. L. Sohn, and M. Tinkham, *ibid.* **43**, 8682 (1991); M. Y. Choi, *ibid.* **46**, 564 (1992); S. J. Lee and T. C. Halsey, *ibid.* **47**, 5133 (1993).
- ¹⁴H. Eikmans and J. E. van Himbergen, Phys. Rev. B **44**, 6937 (1991); **41**, 8927 (1990).
- ¹⁵D. Domínguez, J. V. José, A. Karma, and C. Wiecek, Phys. Rev. Lett. **67**, 2367 (1991); D. Domínguez and J. V. José, Phys. Rev. B **48**, 13 717 (1993).
- ¹⁶D. Domínguez and J. V. José, Phys. Rev. Lett. **69**, 514 (1992).
- ¹⁷A discussion of the effects of the long-range full inductance matrix in the subharmonic Shapiro steps can be found in D. Domínguez and J. V. José, Int. J. Mod. Phys. B **8**, 3749 (1994).
- ¹⁸G. Chu and J. V. José, Phys. Rev. B **47**, 8365 (1993); see also J. V. José, D. Domínguez, and G. Chu, in *Proceedings of the 2nd CTP Workshop on Statistical Physics: KT Transition and Superconducting Arrays* (Ref. 2).
- ¹⁹C. J. Lobb, D. W. Abraham, and M. Tinkham, Phys. Rev. B **27**, 150 (1983).
- ²⁰K. Nakajima and Y. Sawada, J. Appl. Phys. **52**, 5732 (1981).
- ²¹A. Majhofer, T. Wolf, and W. Dieterich, Phys. Rev. B **44**, 9634 (1991).
- ²²P. Minnhagen, Phys. Rev. B **23**, 5745 (1981).
- ²³D. Stroud and S. Kivelson, Phys. Rev. B **35**, 3478 (1987).
- ²⁴J. Pearl, Appl. Phys. Lett. **5**, 65 (1964).
- ²⁵T. P. Orlando, J. E. Mooij, and H. S. J. van der Zant, Phys. Rev. B **43**, 10 128 (1991).
- ²⁶J. R. Phillips, H. S. J. van der Zant, J. White, and T. P. Orlando, Phys. Rev. B **47**, 5219 (1993).
- ²⁷J. R. Phillips, H. S. J. van der Zant, J. White, and T. P. Orlando, Phys. Rev. B **50**, 9387 (1994).
- ²⁸J. R. Phillips, H. S. J. van der Zant, J. White, and T. P. Orlando, Phys. Rev. B **50**, 9380 (1994).
- ²⁹D. Reinell, W. Dieterich, T. Wolf, and A. Majhofer, Phys. Rev. B **49**, 9118 (1994); A. Majhofer (private communication).
- ³⁰T. Hagenaaers *et al.* (unpublished).
- ³¹S. Lachenmann *et al.* (unpublished).
- ³²Y. Y. Wang, R. Rammal, and B. Pannetier, J. Low Temp. Phys. **68**, 301 (1987).
- ³³J. Castro and A. López, Phys. Rev. B **46**, 1075 (1992).
- ³⁴J. Castro, Ph.D. thesis, Instituto Balseiro, Bariloche, Argentina, 1992; J. Castro and A. López (unpublished).
- ³⁵H. Frahm, S. Ullah, and A. T. Dorsey, Phys. Rev. Lett. **66**, 3067 (1991); F. Liu, M. Mondello, and N. Goldenfeld, *ibid.* **66**, 3071 (1991); R. Kato, Y. Enomoto, and S. Maekawa, Phys. Rev. B **44**, 6916 (1991); M. Machida and H. Kaburaki, Phys. Rev. Lett. **71**, 3206 (1993).
- ³⁶T. Chen and S. Teitel, Phys. Rev. Lett. **74**, 2792 (1995); G. Carneiro, *ibid.* **75**, 521 (1995).
- ³⁷H. S. Bokil and A. P. Young, Phys. Rev. Lett. **74**, 3021 (1995).
- ³⁸D. Domínguez, E. A. Jagla, and C. A. Balseiro, Phys. Rev. Lett. **72**, 2773 (1994).
- ³⁹J. V. José and G. Chu, Bull. Am. Phys. Soc. **39**, 378 (1994); and (unpublished).
- ⁴⁰A preliminary account of this work, for diagonal and nearest-neighbors inductance matrices, has been given in D. Domínguez and J. V. José, Bull. Am. Phys. Soc. **37**, 61 (1992). See also D. Domínguez, Ph.D. thesis, Instituto Balseiro, Bariloche, Argentina, 1992.
- ⁴¹C. P. Bean, Phys. Rev. Lett. **8**, 250 (1962); Rev. Mod. Phys. **36**, 31 (1964).
- ⁴²A. A. Abrikosov, L. P. G'orkov, and I. Ye. Dzyalosinskii, *Quantum Field Theoretical Methods in Statistical Physics*, 2nd ed. (Pergamon Press, New York, 1965), p. 253.
- ⁴³Note that in Ref. 16 we used τ_{Φ}^* instead of τ_{Φ} as the characteristic magnetic time scale.
- ⁴⁴P. G. de Gennes, *Superconductivity of Metals and Alloys* (Addison-Wesley, Redwood City, 1966).
- ⁴⁵S. Teitel and C. Jayaprakash, Phys. Rev. Lett. **51**, 1999 (1983); T. C. Halsey, Phys. Rev. B **31**, 5728 (1985).
- ⁴⁶L. Jacobs and C. Rebbi, Phys. Rev. B **19**, 4486 (1979); L. Kramer, *ibid.* **3**, 3821 (1971).
- ⁴⁷M. Tinkham, Phys. Rev. **129**, 2413 (1963); A. L. Fetter and P. C. Hohenberg, *ibid.* **159**, 330 (1967).
- ⁴⁸A. H. Silver and J. M. Zimmerman, Phys. Rev. **157**, 317 (1967).
- ⁴⁹W. H. Press, B. P. Flannery, S. A. Teukolsky, and W. T. Vetterling, *Numerical Recipes* (Cambridge University Press, Cambridge, England, 1989).
- ⁵⁰C. W. Gear, *Numerical Initial Value Problems in Ordinary Differential Equations* (Prentice-Hall, Englewood Cliffs, NJ, 1971).
- ⁵¹C. Temperton, J. Comput. Phys. **34**, 314 (1980), and references therein.
- ⁵²L. A. Hageman and D. M. Young, *Applied Iterative Methods*, (Academic Press, Orlando, 1981).